The influence of radiative heat transfer on flame propagation in dense iron-air aerosols

Ramaekers, W. J.S.; Hazenberg, T.; Thijs, L. C.; Roekaerts, D. J.E.M.; van Oijen, J. A.; de Goey, L. P.H.

DOI
10.1016/j.combustflame.2024.113848

Publication date
2025

Document Version
Final published version

Published in
Combustion and Flame

Combustion and Flame 272 (2025) 113848

Contents lists available at ScienceDirect

Combustion and Flame

journal homepage: www.sciencedirect.com/journal/combustion-and-flame

The influence of radiative heat transfer on flame propagation in dense iron-air aerosols

W.J. S. Ramaekers [a], T. Hazenberg [a,*], L.C. Thijs [a], D.J.E.M. Roekaerts [b], J.A. van Oijen [a], L.P.H. de Goey [a]

[a] Eindhoven University of Technology, Groene Loper 3, 5612 AE Eindhoven, The Netherlands
[b] Delft University of Technology, Mekelweg 5, 2628 CD Delft, The Netherlands

ARTICLE INFO

Keywords:
Zero-emission energy carrier
Metal fuel
Iron aerosol
Flame speed
Radiative heat transfer

ABSTRACT

It is demonstrated that in the (near) zero-gravity experiments conducted by Tang et al. (Combust. Flame; 2009, 2011) iron powder aerosols created using the finest powders are optically thick, implying that radiative heat transfer between particles should not be neglected. To test this concept, an iron particle oxidation model has been implemented in OpenFOAM, including a coupling with the P1-model for radiative heat transfer.

For flame simulations in which radiation is not included, obtained flame propagation velocities deviate less than 8% with results obtained using Chem1D-Fe and also show a good correspondance with algebraic models for optically thin aerosols. No significant difference in predicted flame propagation velocity is observed between 1D and 3D simulations: contrary to what is seen in gaseous flames, including the curvature of the flame does not increase predicted flame speeds substantially. However, measured flame propagation velocity values exceed numerically obtained predictions excluding thermal radiation by a factor of three to four. To the authors' knowledge, this discrepancy is exemplary for the difference between experimentally obtained values for flame propagation velocities, and predictions made using numerical simulation tools neglecting radiative heat transfer.

Accounting for radiation increases predicted flame propagation velocities, in the absence of confining boundaries, by approximately a factor of 10 which is in line with algebraic models for optically thick aerosols. In 3D simulations for the two finest iron powders in the experiments, including radiation and accounting for the presence of the confining tube wall results in an error of 11% and 35% with respect to measured flame propagation velocities, significantly smaller than predictions obtained excluding thermal radiation. Although these flames are not purely radiation-driven, inclusion of particle-to-particle radiative heat transfer enhances flame propagation velocities in simulations to values that correspond much better with experimental values than if radiation would not be taken into account.

1. Introduction

In the last two decades metal powders have been investigated as recyclable energy carriers as they have a volumetric energy density comparable to hydrocarbon fuels [1,2]. Metal powders have been proposed due to the inherent absence of carbon- and sulphur-oxides in combustion products, their high (volumetric) energy density and their straightforward storage over extended periods of time. In metal-fuel combustion, micron-sized metal particles are burnt in heterogeneous flames to supply thermal power to industrial processes. Closed-loop metal-fuel cycles can be achieved if all metal can be recollected in its oxidised state to be reduced for use in a subsequent cycle. Reduction of these metal oxides can be performed using excess green electricity, thereby making metal powders renewable replacements for fossil fuels.

In order to facilitate the capture of all metal-containing species in the combustion products, both metal and metal-oxides should remain in their condensed state during the combustion process. Bergthorson et al. [3] introduced a model for single metal particle oxidation and identified two processes creating gaseous species: (1) vapour-phase metal combustion resulting in gaseous metal, and (2) the formation of gaseous metal-oxides. Formation of these gaseous species can be prevented if the particle temperature remains well below the boiling point of both metal and its oxides: Bergthorson et al. pointed out that iron is one of the very few metals which fulfils this requirement. A flame or percolation wave, in which hot burnt particles supply heat to pre-heat and ignite cold unburnt particles, is the most obvious way to sustain the continuous oxidation process of the aerosol. Applications in

* Corresponding author.
E-mail address: t.hazenberg@tue.nl (T. Hazenberg).

https://doi.org/10.1016/j.combustflame.2024.113848
Received 29 April 2024; Received in revised form 1 November 2024; Accepted 8 November 2024
Available online 26 November 2024

which flame propagation in iron aerosols could be exploited range from closed-loop terrestrial power generation to future space propulsion, but understanding these phenomena better could also be of great benefit for preventing dust explosion accidents.

One of the first simplified expressions for the planar flame propagation velocity in aerosols was based on the assumption that the convective and conductive heat flux balance at the interface between the preheat- and combustion zone [4]:

$$u_{f,1} = \sqrt{\frac{\lambda}{\overline{\rho c_p}} \left[\frac{T_{eq} - T_{p,ign}}{T_{p,ign} - T_u} \right] \frac{1}{\tau}}. \quad (1)$$

Here, λ denotes the thermal conductivity of the carrier gas, $\overline{\rho c_p}$ denotes the volumetric specific heat for the discrete and continuous phase combined and τ denotes the particle burn time. T_{eq} denotes the equilibrium temperature of the burnt aerosol, $T_{p,ign}$ denotes the particle ignition temperature and T_u denotes the unburnt aerosol temperature. Extrapolation of experimental observations by Ning et al. [5] leads to $\tau \approx 1.0$ ms for iron particles having a diameter of $d_p = 5$ μm. For a stoichiometric iron-air aerosol (*i.e.* $C_p = 0.956$ kg m^{-3} of Fe powder at 298.15 K and 1 atm, based on conversion of Fe to FeO), a chemical equilibrium calculation leads to $T_{eq} = 2284$ K. Assuming that $T_{p,ign} = 1000$ K, $\overline{\rho c_p} = 1620$ J m^{-3} K^{-1} (air and iron particles combined at 298.15 K and 1 atm) and $\lambda = 0.023$ W m^{-1} K^{-1} (air at identical conditions), leads to an estimated flame propagation velocity of $u_{f,1} = 16.1$ cm s^{-1}. This exemplary value is of the same order of magnitude as experimentally-obtained values, albeit on the low side as will be seen in the next paragraph.

1.1. Previous research on flame speeds in iron aerosols

Flame speeds in gaseous fuel-oxidiser mixtures have been studied for several decades and are now fairly well understood, but flame propagation in metal aerosols has only gained significant attention over the last ten years or so. A concise overview of experiments used to quantify flame front propagation velocities in metal aerosols has recently been published by Goroshin et al. [6].

Sun et al. [7,8] measured flame velocities in spherically expanding iron aerosol flames using two very fine powders ($d_p \in [1, 3]$ μm and $d_p \in [2, 4.5]$ μm) at varying iron particle concentrations ($C_p \in [0.5, 2.0]$ kg m^{-3}). Although quantitative results are hard to use in comparisons due to the ambiguous definition of flame front velocity u_f, it is apparent that for a given C_p the use of finer particles results in higher values for u_f. Furthermore, an increase of u_f with increasing C_p is observed up to $C_p \approx 1.0$ kg m^{-3}, coinciding with the stoichiometric iron particle concentration for the conversion of Fe to FeO. If C_p was subsequently increased from approximately 1.0 to 2.0 kg m^{-3} u_f was observed to decrease but with a reduced sensitivity compared to sub-stoichiometric values of C_p. These trends were consistent between the two used powders.

A decade later, Tang et al. [9,10] measured flame propagation velocities in iron suspensions under near zero-gravity conditions during a parabolic flight campaign. Five different iron powders with arithmetic mean particle diameters $d_{p,10}$ ranging between 3.3 and 33.8 μm and a C_p estimated between 0.9 and 1.3 kg m^{-3} were burned in cylindrical Pyrex tubes having an inner diameter of 4.8 cm; obtained values for u_f in an O_2-N_2 blend representing air ($X_{O_2} = 0.21$) ranged between approximately 7 cm s^{-1} for $d_{p,10} = 33.8$ μm to 56 cm s^{-1} for $d_{p,10} = 3.3$. When N_2 was replaced by He, resulting in a significant increase of both thermal diffusivity $\kappa = \lambda \rho^{-1} c_p^{-1}$ and the diffusion coefficient of oxygen D_{O_2}, values for u_f practically doubled compared to the O_2-N_2 blend. For the coarsest powders the proportionality $u_f \propto \sqrt{\kappa/\tau}$ from Eq. (1) was observed, but for the finest powder, with $d_{p,10} = 3.3$ μm, the increase in u_f was less than expected replacing N_2 by He. This gave rise to the hypothesis that the oxidation rate of small particles is determined by chemical kinetics, while for larger particles diffusive processes are rate-limiting.

Wright et al. [11] also measured flame propagation velocities of an iron powder in O_2-N_2 blends in which X_{O_2} was increased from 0.15 to 0.60. A very fine powder with a $d_{p,32} = 2.5$ μm was used at an estimated C_p of 0.6 kg m^{-3}. Since the sedimentation velocity (≈ 1.6 mm s^{-1}) in this terrestrial set-up was two to three orders of magnitude smaller than the flame propagation velocity it could safely be neglected. It was computed that these flames predominantly fell in the continuous combustion regime, and u_f exhibited a nearly linear proportionality with X_{O_2} in the carrier gas. Flame propagation in these aerosols was concluded not to be limited by conduction of heat but rather by the particle oxidation rate; the strong dependency on X_{O_2} most likely indicates that this oxidation process is still limited by the diffusion of O_2 towards the particle surface rather than chemical kinetics. Obtained values for u_f ranged between approx. 40 cm s^{-1} for $X_{O_2} = 0.15$ to 80 cm s^{-1} for $X_{O_2} = 0.60$. In these results the proportionality $u_f \propto \sqrt{1/\tau}$ from Eq. (1) could be distinguished assuming that combustion was limited by diffusion of O_2 towards the particle and that $\tau \propto 1/X_{O_2}$.

Very recently, Fedoryk et al. [12] used a Bunsen flame set-up to determine the burning velocity of a fine iron powder in air. The used powder was reported to have a narrow size distribution with $d_{p,10} = 12.7$ μm and C_p was varied between 0.42 and 0.96 kg m^{-3}. Its upper value is quasi stoichiometric for the conversion of Fe to FeO and in the range for C_p reported by Tang and co-workers. The obtained value for $u_f = 14$ cm s^{-1} showed no significant dependence on C_p. This value is in line with results of Tang et al. but does not show the correlation between C_p and u_f as reported by Sun et al. for sub-stoichiometric aerosols.

From the experiments several regimes are hypothesised in which the rate-determining mechanism of flame propagation is different: for small particles surface chemistry is expected to be rate-limiting, while for large particles the diffusion of oxygen and heat is rate-determining. C_p also seems to play a significant role: for low values of C_p thermal diffusion between particles is the limiting mechanism. Replacement of N_2 in the carrier gas by gasses having lower thermal diffusivities, like Ar or Xe, amplifies thermal diffusion being the rate-determining process. For elevated values of C_p, or the replacement of N_2 by a gas having a higher thermal diffusivity like He, the heat-release rate of the particle is expected to be rate-determining [13].

In parallel with the experiments, numerical simulation tools for flame propagation in iron aerosols have been developed over the last years. Besides implementations in 3D CFD codes (this work, [14]), 1D flame codes have been developed for iron aerosol combustion at McGill University [15], TU Darmstadt [16] and at Eindhoven University of Technology (Chem1D-Fe, for details see [17]). Aside from the uncertainty in C_p in experiments, values for u_f obtained in simulations typically are much smaller than experimentally obtained values. Hazenberg et al. [17] report values for u_f between 1 and 10 cm s^{-1} for stoichiometric 1D flames with $2 \leq d_p \leq 20$ μm. Without scrutinising all details of these two simulation codes it needs to be noted that predictions made by these, independently created, numerical codes are not very different: for a stoichiometric, mono-disperse iron dust flame with $d_p = 10$ μm, Soo et al. [15] report a u_f of approx. 5 cm s^{-1} while Hazenberg et al. predict 6.9 cm s^{-1}. Although Eq. (1) makes use of a few assumptions that are generally not entirely justified [6], a good correspondence is observed between predictions made using Eq. (1) and Chem1D-Fe: the latter predicts $u_f = 13.3$ cm s^{-1} for the stoichiometric mono-disperse aerosol with $d_p = 5$ μm where Eq. (1) predicted $u_f = 16.1$ cm s^{-1}.

To show the disparity between measurements and simulations, the experiments by Tang et al. [9] were simulated using Chem1D-Fe. Particle Size Distributions (PSDs) consisting of 10 bins were reconstructed from reported values for $d_{p,10}$ and $d_{p,32}$ assuming a Rosin-Rammler distribution; for C_p values of 0.9, 1.1 and 1.3 kg m^{-3} have been used, corresponding to the lower limit, the mean and the upper limit of the certainty interval of the experiments. Radiative heat transfer is excluded in these simulations. Fig. 1 depicts this dissimilarity: u_f from

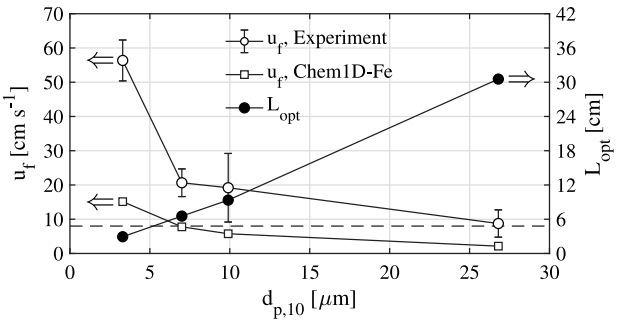

Fig. 1. Flame propagation velocity for experiments by Tang et al. : open circles with errorbars represent measured mean and RMS values while open squares show simulation results using Chem1D-Fe for C_p = 1.1 kg m^{-3}. Solid circles represent L_{opt}, computed using Eq. (3), and the dashed horizontal line indicates the inner tube diameter in the experiment.

experiments exceed numerically obtained values by a factor of two to three, and this disparity seems to increase for the finest iron powder. Lowering C_p to 0.9 kg m^{-3} in the simulations increased u_f by less than 5% while increasing C_p to 1.3 kg m^{-3} lowered u_f by less than 5%. Errorbars for these cases have been omitted since they fall within the solid symbols. Tang et al. present an analytical 1D model in their publication [9] and include a correction factor equal to 2 to account for flame front curvature of these flames. This is a well-known effect in gas-phase flames, however, not yet validated for iron dust flames. In Section 3.5 it will be examined whether spherical aerosol flames in tubes indeed progress with higher u_f values than 1D flat flames do. All in all, it is concluded that simulation codes consistently underestimate experimentally-obtained flame propagation velocities in iron dust flames, even when the large spread of experimental results among themselves is taken into consideration.

1.2. Might thermal radiation play a role of importance?

Whereas Eq. (1) assumes conduction to be the dominant heat transfer mechanism, considering the T_{eq} of 2284 K, one might just as well assume radiative heat transfer to be the dominant heat exchange mechanism. The latter assumption results in a balance between the convective heat flux required to heat particles from T_u to $T_{p,ign}$ and the radiative heat flux emitted by the hot particles which can be restated to [18]:

$$u_{f,2} = \frac{\epsilon_p \sigma T_{eq}^4}{\overline{\rho c_p}\left(T_{p,ign} - T_u\right)}, \tag{2}$$

in which ϵ_p denotes particle emissivity and σ denotes the Stefan–Boltzmann coefficient. Assuming ϵ_p = 0.7 for liquid FeO [19] leads to $u_{f,2}$ = 95.1 cm s^{-1} for the same iron-air aerosol. In other words, if radiation replaces conduction as the dominant heat transfer mechanism, u_f increases by one order of magnitude.

Eq. (2) assumes that the radiative heat flux is entirely used to heat up unburnt particles, and this introduces the prerequisite that the confinement length scale must be equal to at least several optical attenuation lengths. If this prerequisite is not met, the radiative heat flux is partly lost to the confinement walls or the environment. In aerosols the discrete phase typically determines its radiative properties and the optical attenuation length L_{opt} can be estimated by:

$$L_{opt} = \left[\lim_{V\to 0} \sum_{n=1}^{N_p} \frac{\epsilon_p A_{pp,n}}{V}\right]^{-1}, \tag{3}$$

where A_{pp} denotes the projected surface of particles. For mono-disperse aerosols Eq. (3) reduces to:

$$L_{opt} = \frac{2}{3}\frac{\rho_p d_p}{\epsilon_p C_p} \tag{4}$$

in which ρ_p denotes the density of the condensed phase particles. In Section 2.1 a temperature- and composition-dependent formulation for ρ_p will be introduced, but for the estimations in this section the constant value of 7875 kg m^{-3} (Fe at 293.15 K [20]) is used. Assuming C_p = 1.1 kg m^{-3} and using 5 million random draws from the Rosin-Rammler distribution, predictions for L_{opt} in the experiments by Tang et al. are made using Eq. (3) and are shown in Fig. 1. For the finest powder the obtained value for L_{opt} corresponds to approx. 60% of the inner tube diameter while for the second-finest powder L_{opt} corresponds to approx. 135% of this diameter. This implies that usage of the finest powder results in an optically thick unburnt aerosol, and the second-finest powder results in an aerosol in the transition regime between optically thick and optically thin.

Although no verified laboratory or field experiments substantiate the existence of purely radiation-driven aerosol flames, as pointed out by Goroshin et al. [6], these calculations give rise to the hypothesis that particle–particle radiative heat transfer cannot be neglected straightforwardly for these aerosols, and might (partly) explain the discrepancy between values for u_f obtained in experiments and simulations which exclude the effects of radiative heat transfer.

1.3. Paper objective and structure

This paper has the objective to examine what the contribution of radiative heat transfer is in flames structures in dense aerosols created from very fine iron powders. Section 2 discusses the mathematical model implemented in OpenFOAM, divided into submodels for the discrete phase, continuous phase and radiative heat transfer. Simulation set-ups and results are discussed in Section 3. 1D geometries are treated first since they represent flames which are undisturbed by the presence of confining boundaries. Subsequently, set-ups and results in 3D geometries, requiring more attention to be paid to the prescription of boundary conditions, are discussed. Section 4 summarises all findings and recommendations.

2. Modelling of combustion in iron aerosols

In this study an Euler–Lagrange approach adopted in which the continuous phase, *i.e.* the carrier gas, is governed by the Navier–Stokes equations and the discrete phase, *i.e.* the iron particles, is tracked in time. Sections 2.1 and 2.2 describe the behaviour of the discrete and continuous phase while Section 2.3 treats the model for radiative heat transfer employed in this study. Section 2.4 complements these sections on how all equations are implemented in the numerical code.

2.1. Mathematical model for the discrete phase

To describe combustion behaviour of iron particles, several simplified models have been derived over the last decade. Models by Lam et al. [21,22] relied on Heaviside functions for heat release during combustion, and did not account for particle kinematics and O_2 adsorption. Soo et al. [23] developed a formulation for single particle oxidation in which external diffusion of oxygen to the particle is balanced by chemisorption at the particle surface; this formulation was used to study ignition of aluminium particles. Hazenberg et al. [17] modified this model for iron particles assuming that iron (Fe) is converted to feroxide (FeO):

$$2\,\mathrm{Fe} + \mathrm{O_2} \rightarrow 2\,\mathrm{FeO}\ (+\ 544.07\ \mathrm{kJ})\,. \tag{5}$$

Several other studies included pathways leading to magnetite (Fe_3O_4) and hematite (Fe_2O_3) as oxidation products [24,25]; characteristic values for chemical and physical properties of Fe and its oxides are summarised in Table 1. Full conversion to Fe_3O_4 would theoretically occur for C_p = 0.717 kg m^{-3} of Fe powder in air at 298.15 K and 1 atm but chemical equilibrium calculations indicate that a mixture of FeO and Fe_3O_4 is more likely to be found at this value for C_p. Since

Table 1
Characteristic physical values for iron and its oxides. $C_{p,stoich}$ is computed at 1 atm and 298.15 K; Δh^0 denotes the formation enthalpy per kg of oxide at the same temperature. T_{eq} denotes the isenthalpic chemical equilibrium temperature attained at $C_{p,stoich}$ and an initial temperature of 298.15 K.

	M g mol^{-1}	$C_{p,stoich}$ kg m^{-3}	Δh^0 MJ kg^{-1}	T_m K	Δh_{fus} kJ kg^{-1}	T_{eq} K	T_b K	Δh_{evap} MJ kg^{-1}
Fe	55.845			1809 [27]	247.20		3133 [28]	6.2556
FeO	71.844	0.956	−3.7865	1650 [29]	334.85	2284	3400 [27]	5.8120
Fe_3O_4	231.53	0.717	−4.8303	1870 [29]	596.34	2225	2603[a]	N.A.
Fe_2O_3	159.69	0.637	−5.1616	1682[a]	N.A.	2239	N.A.	N.A.

[a] Chemical equilibrium calculations indicate that Fe_3O_4(l) dissociates into FeO(l) before (full) evaporation and that Fe_2O_3(s) dissociates into Fe_3O_4(s) before melting.

the objective of this study is to predict flame propagation velocities for $0.9 \leq C_p \leq 1.3$ kg m^{-3} the formation of these higher oxides will not be considered in this study. This assumption is substantiated by results from van Gool et al. [26] who reported that the inclusion of Fe_3O_4 and Fe_2O_3 only affects predicted values for u_f at very lean conditions.

Particles are assumed to be perfectly spherical: in their unoxidised state this is confirmed by Scanning Electron Microscope images accompanying experimental studies [5,9] and above their melting point surface tension is assumed to keep particles spherical. The reported immiscibility of L1 and L2 in metallurgy [19], considered to be liquid Fe and liquid FeO respectively, substantiates a core-in-shell configuration consisting of an oxide layer around a core of reactant. The surface area of a particle A_p is related to its mass and composition by:

$$A_p = \left[6\sqrt{\pi} m_p \left(\frac{Y_{p,Fe}}{\rho_{Fe}} + \frac{Y_{p,FeO}}{\rho_{FeO}}\right)\right]^{2/3}, \tag{6}$$

in which m_p denotes the particle mass, $Y_{p,Fe}$ and $Y_{p,FeO}$ denote mass fractions of Fe and FeO in the particle. ρ_{Fe} and ρ_{FeO} refer to the density of these two species which are assumed to depend on temperature only. Particle diameter d_p is related to A_p by the geometric relation: $d_p^2 = \pi^{-1} A_p$. For computational efficiency, second-order temperature-dependent polynomials have been adopted for ρ_{Fe} [20] and ρ_{FeO} [30,31]; polynomial coefficients are stated in Table A.1 and hyperbolic tangent functions are used over an interval of 20 K to ensure smooth numerical behaviour during phase transitions. Polynomial coefficients for Fe correspond well to coefficients proposed in other studies [32–36] although a small variation for $\beta_{\rho,1}$ is reported for liquid Fe. Besides the used data, the authors did not find other reliable density data for FeO in literature, but the currently used data is in line with observations by Mori et al. [37] that liquid iron oxide density decreases as the elemental oxygen fraction increases. Mean particle density ρ_p is obtained by dividing total particle mass m_p by $V_p = (\pi/6)\, d_p^3$.

During oxidation, the particle temperature T_p can deviate significantly from the (local) gas temperature T_g and the adsorption of O_2 will cause Y_{O_2} at the particle surface to deviate from its value in the continuous phase $Y_{O_2,g}$. To account for the effect of this temperature difference on transport properties, it is assumed that a gaseous film layer surrounds the unresolved particles and its temperature T_f is estimated by assuming a film factor α:

$$T_f = \alpha T_p + (1-\alpha)\, T_g. \tag{7}$$

Commonly adopted values for α are 1/2 [38] and 2/3 [17,39,40]; Thijs et al. [41] showed that $\alpha = 2/3$ without explicit corrections for Stefan flow agreed well with results from boundary-layer resolved simulations of single particles. This approach will be used here, thereby avoiding the need to include (iterative) corrections for Stefan flow.

While the particle adsorbs O_2, the mass fraction of O_2 in the film layer near the particle surface Y_{surf,O_2} can attain values of $0 \leq Y_{surf,O_2} \leq Y_{g,O_2}$ where Y_{g,O_2} denotes the O_2 mass fraction in the carrier gas. Since dynamic viscosity μ, κ and D_{O_2} are insensitive to the O_2 mass fraction in N_2/air-blends, these transport properties are evaluated for the carrier gas composition at T_f. The need to update the gas composition of the film layer is thereby circumvented. It needs to be noted that this simplification no longer is justified if N_2 is replaced by previously-mentioned gasses He, Ar en Xe since their values for κ and D_{O_2} are substantially different from those of N_2.

Particle velocity components are now described by three ODEs with subscript i in which g_i denotes a component of the gravity vector:

$$\frac{du_{p,i}}{dt} = \left[\frac{\rho_p - \rho_g}{\rho_p}\right] g_i - \left[\frac{3}{4}\frac{\rho_g C_d}{\rho_p d_p}\right] \left|u_{p,i} - u_{g,i}\right| \left(u_{p,i} - u_{g,i}\right);\ i \in [1,3]. \tag{8}$$

The first term in the RHS of Eq. (8) represents the resulting force of gravity and buoyancy and the second one represents the hydrodynamic drag force. The drag coefficient C_d is given by the empirical correlation derived by Schiller and Naumann [42]:

$$C_d = \left(\frac{24}{Re_p}\right)\left[1 + 0.15\ Re_p^{0.687}\right] \quad \text{for} \quad Re_p \leq 10^3, \tag{9}$$

in which the particle Reynolds number is based on film layer properties, and is defined by $Re_p = \rho_f \mu_f^{-1} d_p \left|\boldsymbol{u}_p - \boldsymbol{u}_g\right|$. For the stoichiometric iron-air aerosol in Section 1 the discrete phase volume fraction equals $1.22 \cdot 10^{-4}$. All aerosols in cited works have very similar volume fraction values and two-way coupling between discrete and continuous phase is appropriate [43]. The ideal gas law is used to compute ρ_f in which the mean molecular mass from the carrier gas is used. μ_f is computed using Sutherland's Law in which $\bar{\beta}_{\mu,1}$ and $\bar{\beta}_{\mu,2}$ are mass fraction weighted coefficients:

$$\mu_f = \bar{\beta}_{\mu,1}\left[\frac{T_f^{3/2}}{T_f + \bar{\beta}_{\mu,2}}\right] \quad \text{with} \quad \bar{\beta}_{\mu,m} = \sum_{k=1}^{N_s} \beta_{\mu,k,m} Y_{g,k};\ m \in [1,2]. \tag{10}$$

Coefficients $\beta_{\mu,k,m}$ have been computed using Cantera [44] for pure gasses between 300 and 3000 K and subsequently fit to Eq. (10); both Lennard-Jones parameters and coefficients $\bar{\beta}_{\mu,m}$ are given in Table A.2.

Particle mass is altered by adsorption of O_2 required for the oxidation of Fe, and by evaporation of Fe and FeO:

$$\frac{dm_p}{dt} = \left.\frac{dm_p}{dt}\right|_{ads} + \sum_{k=Fe,FeO} \left.\frac{dm_p}{dt}\right|_{evap,k}, \tag{11}$$

where source terms have positive contributions if they contribute to an increase in m_p and subscript k refers to Fe and FeO. In previous studies it was shown that Knudsen effects in the boundary layer of particles only play a very minor role for the ignition of aluminium, magnesium and boron particles with $d_p \gtrapprox 20$ μm [45] and iron particles with $d_p \gtrapprox 30$ μm [46]. Thijs et al. [47] calculated that the burn time of iron particles is underestimated by less than 10% for iron particles having a $d_p \gtrapprox 10$ μm due to neglecting non-continuum effects in transport phenomena. Based on these findings it is assumed that the particle film layer is adequately described as being a continuum. O_2 adsorption is governed by instantaneous balance between the diffusive flux towards the particle and the consumption rate by the surface reaction given in Eq. (5). Considering that both the diffusive flux and surface reactions are driven by concentrations (and its gradients) rather than mass fractions, the adsorption rate of O_2 can be expressed by:

$$\left.\frac{dm_p}{dt}\right|_{ads} = M_{O_2} A_p r_{d,O_2} \left[\frac{p}{R_u T_f}\right] X_{g,O_2} Da^\star \tag{12}$$

in which $Da^\star$ denotes the normalised Damköhler number:

$$Da^\star = \left[\frac{A_r r_r}{A_r r_r + A_p r_{d,O_2} T_p T_f^{-1}}\right]. \tag{13}$$

This formulation differs slightly from the formulation used by Hazenberg et al. [17] in which O_2 mass fractions were used. $Da^\star$ in Eq. (13) has two limits: if chemical kinetics are much slower than diffusive transport, *i.e.* $A_r r_r \ll A_p r_{d,O_2}$, it is said that particle mass growth is *kinetically-limited* and $Da^\star \approx 0$. At high temperatures chemical kinetics are much faster than diffusive transport, *i.e.* $A_r r_r \gg A_p r_{d,O_2}$, and it is said that particle mass growth is *diffusion-limited*; for the latter case applies that $Da^\star \approx 1$. The reactive surface A_r is defined as: $A_r = A_{Fe} = \left[6\sqrt{\pi} m_p Y_{p,Fe} \rho_{Fe}^{-1}\right]^{2/3}$.

A complex particle ignition model, like the one proposed by Mi et al. [48] for example, is not considered to be required since only (quasi) steady-state aerosol flames are considered here. Furthermore, a computationally expensive ignition model would be prohibitive for some of the envisioned simulations in this study. The reaction rate r_r for reaction (5) is thus closed by a simple, computationally inexpensive Arrhenius expression:

$$r_r = k \exp\left(-T_A/T_p\right), \tag{14}$$

in which k denotes the pre-exponential factor and T_A the activation temperature. To the author's knowledge no experimental data is available allowing an accurate deduction of values for k and T_A, and values proposed by Hazenberg et al. [17] ($k = 75.0 \cdot 10^5$ m s^{-1} and $T_A = 14.4 \cdot 10^3$ K) are adopted in this study. The diffusive transport rate r_{d,O_2} is determined by making use of the Ranz-Marshall correlation [49] to determine the Sherwood-number for O_2:

$$r_{d,O_2} = \frac{Sh_{O_2} D_{f,O_2}}{d_p} \quad \text{with} \quad Sh_{O_2} = 2 + 0.6\, Re_p^{1/2}\, Sc_{O_2}^{1/3}. \tag{15}$$

The Schmidt number for O_2 in the film layer is defined as: $Sc_{O_2} = \mu_f \rho_f^{-1} D_{f,O_2}^{-1}$ and D_{f,O_2} is directly coupled to the other film layer properties via the assumption of a constant Lewis number for O_2 ($Le_{O_2} = 1.114$). The thermal conductivity coefficient λ_f of the film layer is estimated using the modified Eucken correlation [50]:

$$\lambda_f = \mu_f \left[1.32 c_{v,f} + 1.77 R_u \overline{M_f}^{-1}\right], \tag{16}$$

in which $c_{v,f}$ denotes the mixture-averaged specific heat at constant volume of the film layer. The rate of change in Fe mass in the particle can be expressed as:

$$\frac{d}{dt}\left(m_p Y_{p,Fe}\right) = -\left(2 M_{Fe}/M_{O_2}\right) \left.\frac{dm_p}{dt}\right|_{ads} + \left.\frac{dm_p}{dt}\right|_{evap,Fe}, \tag{17}$$

while the mass fraction of FeO follows from the identity $Y_{p,FeO} = 1 - Y_{p,Fe}$.

Spatial variations of T_p within a particle are assumed to be small enough to be neglected: this hypothesis will be verified in *a-posteriori* analysis in Section 3.3. Taking into account convective and radiative heat transfer, heat release due to exothermic surface reactions as well as mass adsorption and evaporation, the evolution of T_p can be described by:

$$m_p c'_{p,p} \frac{dT_p}{dt} = k_c A_p \left(T_g - T_p\right) + Q_{p,reac} + Q_{p,rad} + \sum_{k=Fe,FeO} \left.\frac{dm_p}{dt}\right|_{evap,k} \Delta h_{evap,k}, \tag{18}$$

in which the same summation is used as in Eq. (11). Similar to Eq. (15), the convective heat transfer rate k_c is determined using the Ranz-Marshall correlation by replacing D_{f,O_2} by λ_f and Sc_{O_2} by the film Prandtl number $Pr_f = \mu_f c_{p,f} \lambda_f^{-1}$.

To account for the latent heat in solid-to-liquid transitions (and vice-versa) of both Fe and FeO, the enthalpy of fusion Δh_{fus} is added to the thermodynamic specific heat c_p over a pre-defined temperature interval ΔT_{fus}:

$$c'_p\left(T_p\right) = c_p\left(T_p\right) + \left[H\left(T_p - T_m + \frac{\Delta T_{fus}}{2}\right) - H\left(T_p - T_m - \frac{\Delta T_{fus}}{2}\right)\right] \frac{\Delta h_{fus}}{\Delta T_{fus}}, \tag{19}$$

in which H denotes a hyperbolic tangent function to ensure a continuous and smooth behaviour. Due to the irregular behaviour of c_p for the solid phase of Fe predicted by the 9-coefficient polynomials by McBride et al. [29], temperature-averaged c_p-value for Fe and FeO have been computed between 275 K and T_m for the solid phase and between T_m and T_b for the liquid phase. In the numerical simulations $c_p\left(T_p\right)$ is replaced by its temperature-averaged value $\overline{c_p}$ for increased numerical stability and reduced computational cost. Finally, $c'_{p,p}$ is defined as the mass-weighted values of c'_p for Fe and FeO. The heat release in Eq. (18) due to the (exothermic) surface reaction is given by:

$$Q_{p,reac} = -\left(2\frac{M_{FeO}}{M_{O_2}}\right) \Delta h^0_{FeO} \left.\frac{dm_p}{dt}\right|_{ads} \tag{20}$$

where Δh^0_{FeO} is adopted from Table 1. Since $\int_{300}^{T_m} \left(\overline{c_{p,FeO}} - \overline{c_{p,Fe}}\right) dT$ constitutes to less than 5% of Δh^0_{FeO}, the sensible enthalpy contribution is omitted from $Q_{p,reac}$. Hereby the heat release rate is directly linked to the oxygen adsorption rate by a constant multiplication factor.

Both Eqs. (11) and (18) contain a contribution due to evaporation of Fe and FeO. Chemical equilibrium calculations have been used to compute the partial pressure of Fe(g), FeO(g) and FeO_2(g) in Fe(l) and FeO(l) as a function of temperature. For Fe(l) conservation of elements prescribes that only Fe(g) can have a non-zero partial pressure, for FeO(l) all three gaseous species have non-zero partial pressures. Since the partial pressure of FeO_2(g) is approximately two orders of magnitude smaller than for Fe(g) and FeO(g), the formation of FeO_2(g) is neglected in this study. Evaporation of Fe and FeO from particles is modelled by Raoult's Law following Thijs et al. [51]:

$$\left.\frac{dm_p}{dt}\right|_{evap,Fe} = -\frac{M_{Fe} A_{Fe}}{R_u T_f} r_{d,Fe}\left(p_{vap,I} - p X_{g,Fe}\right) \tag{21}$$

$$\left.\frac{dm_p}{dt}\right|_{evap,FeO} = -\frac{M_{FeO} A_p}{R_u T_f}\left[r_{d,Fe}\left(p_{vap,II} - p X_{g,Fe}\right) + r_{d,FeO}\left(p_{vap,III} - p X_{g,FeO}\right)\right] \tag{22}$$

in which the diffusive transport rates $r_{d,Fe}$ and $r_{d,FeO}$ are determined using Eq. (15) in which constant Lewis numbers for gaseous Fe(g) and FeO(g) are used. $p_{vap,I}$, $p_{vap,II}$ and $p_{vap,III}$ represent vapour pressures of Fe(g) in Fe(l), Fe(g) in FeO(l) and FeO(g) in FeO(l). Evaporation of Fe in Eq. (21) implies the assumption that liquid Fe in the core of particles can evaporate through the liquid FeO shell, which is justified to the authors' opinion by the fact that vapour pressures of Fe(g) in Fe(l) are $\mathcal{O}(10^2)$ times larger than vapour pressures of Fe(g) or FeO(g) in FeO(l). These vapour pressures have been calculated using chemical equilibrium computations [52] and cast in the formula:

$$p_{vap}\left(T_p\right) = \exp\left[\beta_{vap,1} + \beta_{vap,2} T_p^{-1} + \beta_{vap,3} \log T_p\right]. \tag{23}$$

Numerical values for $\beta_{vap,m}$ are stated in Table A.3 and resulting vapour pressures are shown in graph 2 together with their original chemical equilibrium data.

Iron particles for metal fuel cycles typically have diameters ranging from a few μm in well-defined academic experiments to approximately hundred μm in envisioned industrial applications. This implies that even combustion volumes of small lab-scale experiments contain several millions of individual particles: for stoichiometric combustion of iron particles with $d_p = 25$ μm at standard conditions, each m^3 contains $\mathcal{O}(10^{10})$ individual particles. Unless stated otherwise, particles are tracked individually to avoid artificial lumping of local particle-induced effects. If particle numbers in simulations become prohibitive, particles are clustered in parcels to alleviate computational requirements.

2.2. Mathematical model for the continuous phase

The continuous phase is modelled as a compressible Newtonian fluid and subscript g makes the distinction with the discrete phase indicated by the subscript p. The transport equations adopted in this

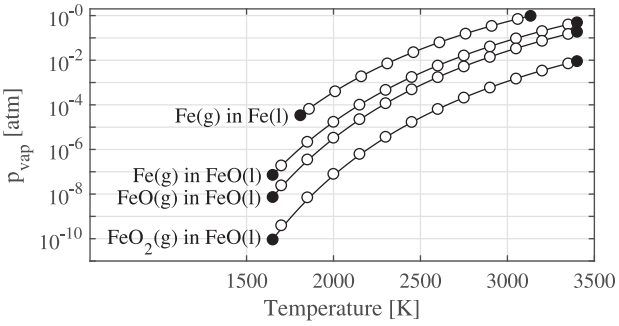

Fig. 2. Vapour pressures of gaseous iron(-oxides) in Fe(l) and FeO(l). Closed circular markers indicate T_m and T_b, open circular markers represent results obtained using Cantera and solid black lines represent the fit through Eq. (23).

study describe the conservation of mass, momentum, species mass fractions $Y_{g,k}$ for species k and sensible enthalpy $h_{s,g}$:

$$\frac{\partial \rho_g}{\partial t} + \frac{\partial \rho_g u_{g,j}}{\partial x_j} = Q_{\text{mass}}, \tag{24}$$

$$\frac{\partial \rho_g u_{g,i}}{\partial t} + \frac{\partial \rho_g u_{g,i} u_{g,j}}{\partial x_j} = -\frac{\partial p}{\partial x_i} + \frac{\partial \tau_{ij}}{\partial x_j} + \rho_g g_i + Q_{\text{mom},i};\ i \in [1,3], \tag{25}$$

$$\frac{\partial \rho_g Y_{g,k}}{\partial t} + \frac{\partial \rho_g u_{g,j} Y_{g,k}}{\partial x_j} = \frac{\partial}{\partial x_j}\left[\rho_g \mathcal{D}_{g,k} \frac{\partial Y_{g,k}}{\partial x_j}\right] + Q_{\text{sp},k};\ k \in \left[1, N_s - 1\right], \tag{26}$$

$$\frac{\partial \rho_g h_{s,g}}{\partial t} + \frac{\partial \rho_g u_{g,j} h_{s,g}}{\partial x_j} = \frac{\partial p}{\partial t} + u_{g,j}\frac{\partial p}{\partial x_j} + \frac{\partial}{\partial x_j}\left[\frac{\lambda_g}{c_{p,g}} \frac{\partial h_{s,g}}{\partial x_j}\right] + Q_{\text{enth}}, \tag{27}$$

where the Einstein summation convention is used over index j. Preferential diffusion effects and viscous dissipation have been neglected and gas-phase chemical kinetics are not taken into account. Conservation of mass is ensured by computing the mass fraction of the abundant species, typically N_2 when air is considered as oxidiser, using the identity $Y_{g,N_s} = 1 - \sum_{k=1}^{N_s-1} Y_{g,k}$ instead of solving Eq. (26). τ_{ik} denotes the viscous stress tensor for a compressible Newtonian fluid:

$$\tau_{ik} = \mu_g \left(\frac{\partial u_{g,i}}{\partial x_k} + \frac{\partial u_{g,k}}{\partial x_i} - \frac{2}{3}\frac{\partial u_{g,j}}{\partial x_j}\delta_{ik}\right), \tag{28}$$

in which δ_{ik} denotes the Kronecker delta. The dynamic viscosity μ_g and thermal conductivity λ_g are computed using Eqs. (10) and (16) in which film properties are replaced by gas phase properties. $c_{p,g}$ is computed using the 7-coefficient thermodynamic polynomials by McBride et al. and $\mathcal{D}_{g,k}$ is calculated assuming constant Lewis numbers, identical to the procedure for film layer. The carrier gas is assumed to behave like a perfect gas and the ideal gas law thereby complements this system of equations. Eqs. (24)–(27) are closed by source terms that result from the two-way coupling between the continuous and discrete phase:

$$Q_{\text{mass}} = -\sum_{n=1}^{N_p}\left(\left.\frac{\mathrm{d}m_{p,n}}{\mathrm{d}t}\right|_{\text{ads}} + \left.\frac{\mathrm{d}m_{p,n}}{\mathrm{d}t}\right|_{\text{evap,Fe}} + \left.\frac{\mathrm{d}m_{p,n}}{\mathrm{d}t}\right|_{\text{evap,FeO}}\right)\boldsymbol{\delta}\left(\boldsymbol{x} - \boldsymbol{x}_n\right), \tag{29}$$

$$Q_{\text{mom},i} = -\sum_{n=1}^{N_p} m_{p,n}\frac{\mathrm{d}u_{p,i,n}}{\mathrm{d}t}\boldsymbol{\delta}\left(\boldsymbol{x} - \boldsymbol{x}_n\right), \tag{30}$$

$$Q_{\text{sp},k} = -\sum_{n=1}^{N_p}\left(\left.\frac{\mathrm{d}m_{p,k,n}}{\mathrm{d}t}\right|_{\text{ads}} + \left.\frac{\mathrm{d}m_{p,k,n}}{\mathrm{d}t}\right|_{\text{evap}}\right)\boldsymbol{\delta}\left(\boldsymbol{x} - \boldsymbol{x}_n\right), \tag{31}$$

$$Q_{\text{enth}} = -\sum_{n=1}^{N_p} k_c A_{p,n}\left(T_g - T_{p,n}\right)\boldsymbol{\delta}\left(\boldsymbol{x} - \boldsymbol{x}_n\right). \tag{32}$$

The multidimensional Dirac function, denoted by $\boldsymbol{\delta}$, indicates that source terms act only at the location of iron particle n; this variable has the unit m^{-3} in 3D geometries. Eqs. (30) and (32) formally also contain contributions due to adsorption and evaporation: since these terms are considered to be very small, they have been omitted in this study. Eq. (31) only has non-zero contributions for O_2, Fe and FeO which are given by Eqs. (13), (21) and (22); other species are not exchanged between discrete and continuous phase. Further oxidation of gaseous Fe and FeO to FeO_2 is not considered in this study.

2.3. Modelling thermal radiation

In Section 1 it was shown that the optical attenuation length L_{opt} for near-stoichiometric aerosols of fine iron powders ranges from just a few to several cm. This is much smaller than the absorption length of the carrier gas, even more so because radiatively most active species in hydrocarbon combustion, CO_2, CO and H_2O, are absent in iron aerosols. The particulate phase thus dominates the radiative properties of the mixture (Liberman [53], Chapter 16) and it can be assumed that the continuous phase is transparant for thermal radiation. This explains why Eq. (27) lacks a source term due to radiation: radiative heat transfer is fully governed by the exchange between particles themselves and confining walls.

The interaction between emission, absorption and scattering of radiation is described by a Radiative Transfer Equation (RTE, *e.g.* Modest [54], Eq. (1.63)). The P_1-model was selected as the solution method for the RTE because it requires modest computational resources compared to more complex models like the Discrete Ordinates Method. Furthermore, this model is expected to be fairly accurate in a medium with a near-isotropic radiation intensity field as generated by optically-thick aerosols. A relevant limitation of the P_1-model is that, because of the restrictions in the allowed shape of the radiation intensity as function of directional coordinates, can only be combined with the simplest formulations of the scattering function being homogeneous and linear anisotropic phase functions [54]. In the P_1-model the radiative heat flux is proportional to the gradient of the total incident radiation field G, with unit $\mathrm{W\,m^{-2}}$, and the radiative properties of the particle cloud:

$$q_{\text{rad},i} = -\left(\frac{1}{3a_p + 3\sigma_p - \beta_{\text{scat}}\sigma_p}\right)\frac{\partial G}{\partial x_i}. \tag{33}$$

Here a_p and σ_p denote the optical absorption and scattering coefficient of the dust cloud and are determined by the projected surface area A_{pp} and surface emissivity ϵ_p of the particles:

$$a_p = \sum_{n=1}^{N_p} \epsilon_p A_{pp,n}\boldsymbol{\delta}\left(\boldsymbol{x} - \boldsymbol{x}_n\right), \tag{34}$$

$$\sigma_p = \sum_{n=1}^{N_p} \left(1 - \epsilon_p\right) A_{pp,n}\boldsymbol{\delta}\left(\boldsymbol{x} - \boldsymbol{x}_n\right). \tag{35}$$

For spherical particles A_{pp} is related to A_p by the geometrical relation $A_{pp} = A_p/4$. Eqs. (34) and (35) show the implicit assumption that incoming radiation is either absorbed or scattered, and (direct) transmission is absent; the relative importance of absorption and scattering is controlled by ϵ_p. No spectral dependency for a_p and σ_p is considered, which is justified by the fact that values for d_p in this work are of $\mathcal{O}(10^1)$ µm, and thereby comparable to the upper wavelength limit in infrared radiation. The observant reader may have recognised that a_p, as defined by Eq. (34) is the reciprocal value of L_{opt} in Eq. (3). In Eq. (33) $\beta_{\text{scat}} \in [-1, 1]$ is the coefficient of the linear term in the expansion of the scattering phase function. Negative values of β_{scat} describe cases where scattering in backward directions exceeds scattering in forward directions; $\beta_{\text{scat}} = -1$ represents the linear approximation for the scattering phase function for a diffuse reflecting sphere (see Modest [54], Section 12.9). In the frame of the P_1-model a modification of the choice for β_{scat} is equivalent to a slight change in d_p: adjusting β_{scat} from −1 to 0 in Eq. (33) has the same effect as a change in d_p by a factor $\sqrt{(7 - 4\epsilon_p)/(6 - 3\epsilon_p)} \approx 1.04$. Given the obscurity of the scattering phase function for iron particles, and its minor effect with respect to the variations in d_p, $\beta_{\text{scat}} = 0$ is assumed in this study implying that scattering is independent of angle and thereby facilitating the use of the

P_1-model. Combining Eqs. (33), (34) and (35) show that $q_{\mathrm{rad},i}$ becomes independent of ϵ_p for this choice for β_scat. The RTE now takes the form of the following transport equation for G:

$$-\frac{\partial q_{\mathrm{rad},j}}{\partial x_j} = \frac{\partial}{\partial x_j}\left[\frac{1}{3a_\mathrm{p}+3\sigma_\mathrm{p}}\frac{\partial G}{\partial x_j}\right] = a_\mathrm{p}G - \sum_{n=1}^{N_\mathrm{p}} \epsilon_\mathrm{p} A_{\mathrm{p},n}\sigma_\mathrm{SB} T_{\mathrm{p},n}^4 \boldsymbol{\delta}\left(\boldsymbol{x}-\boldsymbol{x}_n\right), \tag{36}$$

where σ_SB denotes the Stefan–Boltzmann constant and again the Einstein summation convention is used over index j. The first contribution in the RHS of Eq. (36) represents the volumetric heat source caused by the radiation taken up by the particles. The volumetric heat sink, caused by hot radiating particles, is represented by the second contribution in the RHS. When the G-field has been computed, the source term $Q_\mathrm{p,rad}$ in Eq. (18) is calculated using the expression:

$$Q_\mathrm{p,rad} = \epsilon_\mathrm{p} A_\mathrm{pp} G - \epsilon_\mathrm{p} A_\mathrm{p} \sigma_\mathrm{SB} T_\mathrm{p}^4 = \epsilon_\mathrm{p} A_\mathrm{p}\left(\frac{G}{4} - \sigma_\mathrm{SB} T_\mathrm{p}^4\right). \tag{37}$$

Literature reports a wide range for ϵ_p of iron and its oxides: for Fe(s) values have been reported ranging between 0.24 and 0.6 [55,56] and for Fe(l) values between 0.335 and 0.365 [19,55–57] have been reported. For iron oxides values are significantly higher: for solid iron oxides values have been reported ranging between 0.8 and 0.92 [56] and for liquid iron oxides ranging between 0.53 and 0.9 [19,55]. In this work a constant value of $\epsilon_\mathrm{p} = 0.7$ is assumed since the highest values for T_p will be attained when particles are highly-oxidised liquid droplets.

Confining walls are assumed to act as opaque grey diffusive surfaces, allowing the Marshak boundary condition [58] to prescribe the radiative heat flux through these walls:

$$q_\mathrm{rad,w} = -\frac{\epsilon_\mathrm{w}}{4-2\epsilon_\mathrm{w}}\left[4\sigma_\mathrm{SB}T_\mathrm{w}^4 - G_\mathrm{w}\right] \tag{38}$$

where ϵ_w denotes the wall emissivity, T_w refers to the imposed wall temperature boundary condition and G_w is the incident radiation at the wall. Combining Eqs. (33) and (38) leads to a boundary condition for G relating T_w, G and its boundary-normal gradient at the wall. Appendix B shows that for semi-transparent walls, one can analytically derive an expression almost identical to Eq. (38): this substantiates the assumption that the Marshak boundary condition can also be applied to semi-transparent wall. Far-fields in simulations, including open ends of tubes, should be located several optical attenuation lengths away from reacting particles such that the netto radiative heat flux can be assumed to be negligibly small and a zero-gradient boundary for G can be imposed in accordance with Eq. (33).

2.4. Numerical considerations

OpenFOAM employs a Finite Volume (FV) formulation for all transport equations in which volume integrals of source terms in Eqs. (24)–(27) and Eqs. (34)–(35) appear. For the deflagrations to be modelled, a Low-Mach number approximation is used to filter out sound waves, resulting in a Poisson-equation for pressure. Coupling between pressure and velocity fields is achieved by employing the PIMPLE algorithm. In Eq. (26) a correction velocity (see Poinsot et al. [59], Section 1.1.5) is added to $u_{\mathrm{g},j}$ to ensure that $Y_{\mathrm{g},N_\mathrm{s}}$ is correct.

To resolve the incongruity of using discrete contributions in Eqs. (24)–(27) and (36), parameters having the discrete Dirac function $\boldsymbol{\delta}$ in their definition are recast by integrating over FV grid cells [60]:

$$\sum_{n=1}^{N_\mathrm{p}} \int_\mathrm{cell} \psi\,\boldsymbol{\delta}\left(\boldsymbol{x}-\boldsymbol{x}_n\right)\mathrm{d}V = \sum_{n\,\in\,\mathrm{cell}} \psi\left(\boldsymbol{x}_n\right), \tag{39}$$

in which ψ denotes an arbitrary variable; volumetric properties are obtained by dividing by V_cell.

Second-order central differencing schemes have been used to compute spatial derivatives of the continuous phase; a SuperBee flux limiter is included for the convective term in Eq. (25). Time stepping of equations for both discrete and continuous phase is carried out with an (implicit) Euler backward scheme. The numerical error introduced by the first-order temporal discretisation is expected to be significantly smaller than the error introduced by the second-order spatial discretisation schemes since the (constant) time step Δt is limited to several µs to resolve the oxidation of µm-sized particles rather than CFL-number, which is estimated to be of $\mathcal{O}(10^{-2})$ for a grid spacing of 25 µm. Linear interpolation is used when $u_{\mathrm{g},i}$ has to be determined at particle positions; for the other continuous phase properties the cell-centred value is assumed.

Table 2
Parameters of iron powders used in experiments by Tang et al. : λ_RR, k_RR are derived from the given values for $d_\mathrm{p,10}$ and $d_\mathrm{p,32}$. $d_\mathrm{p,min}$ and $d_\mathrm{p,max}$ are the minimal and maximal values for d_p used in simulations.

Powder	$d_\mathrm{p,10}$ µm	$d_\mathrm{p,32}$ µm	λ_RR µm	k_RR –	$d_\mathrm{p,min}$ µm	$d_\mathrm{p,max}$ µm
Powder A	3.3	4.3	3.73	2.65	0.5	8.0
Powder B	7.0	9.6	7.90	2.35	1.0	18.0
Powder C	9.9	13.7	11.18	2.30	1.0	25.0
Powder D	26.8	44.6	30.00	1.70	2.5	100.0

3. Flame propagation simulations

One of the most concise experimental datasets available for the combustion of dense iron aerosols is composed by Tang et al. [9,10]. This dataset is briefly described in Section 3.1 and is used to compare our simulations with. Sections 3.2 and 3.3 discuss the set-up and results for 1D geometries, in which the only relevant coordinate is the one perpendicular to the flat flame front. These simulations allow a direct comparison with previously reported flame structures, and results in predictions for u_f undisturbed by the presence of confining boundaries. In Sections 3.4 and 3.5 the set-up and results for simulations of the actual experiment are discussed. Contrary to the 1D geometries, these simulations contain the confining Pyrex tube as a boundary where Eq. (38) is imposed.

3.1. Outline of experiments by Tang et al.

Tang et al. burned fine iron powders in air under near zero-gravity conditions during a parabolic flight campaign. For the powders used in these experiments an arithmetic ($d_\mathrm{p,10}$) and Sauter mean diameter ($d_\mathrm{p,32}$) is reported as well as their morphology. In the simulations it is assumed that particles are perfectly spherical and that PSDs can be described using a Rosin-Rammler distribution: its scale parameter λ_RR and shape parameter k_RR were calculated such that experimental values of d_{10} and d_{32} are recovered. The resulting PSDs are clipped at $d_\mathrm{p,min}$ and $d_\mathrm{p,max}$ to avoid the presence of very small, fast-burning particles and very large particles containing a disproportionate amount of mass: Ravi et al. [61] have shown that omitting these particles only has very minor effect on predictions for u_f. Ravi et al. also pointed out that for a given d_{10} the standard deviation of the assumed analytical expression for the PSD can cause u_f to vary by as much as 15% in fuel-rich aerosols. In case the PSD is described in a discrete manner, Ravi et al. showed that the use of ten bins or more led to a convergence in u_f-predictions: the use of more bins in the discrete PSD has a negligible effect on the prediction of u_f. Since only d_{10} and d_{32} are available for these experiments under fuel-rich conditions, the authors are aware that inaccuracies in predictions for u_f are to be expected. Table 2 summarises all geometric particle characteristics for all four iron powders used in simulations in this study.

In the experiments, fuel-rich suspensions of iron dust in air were created in a cylindrical Pyrex glass tube having an inner diameter of 48 mm by powder dispersion during 10 s, and subsequently 1 s to let the resulting aerosol settle. Resulting values for C_p were estimated between 0.9 kg/m^3 and 1.3 kg/m^3 [10], corresponding to $0.94 \leq \phi \leq 1.36$ for oxidation of Fe to FeO. At $C_\mathrm{p} = 1.1$ kg m^{-3} mean inter-particle

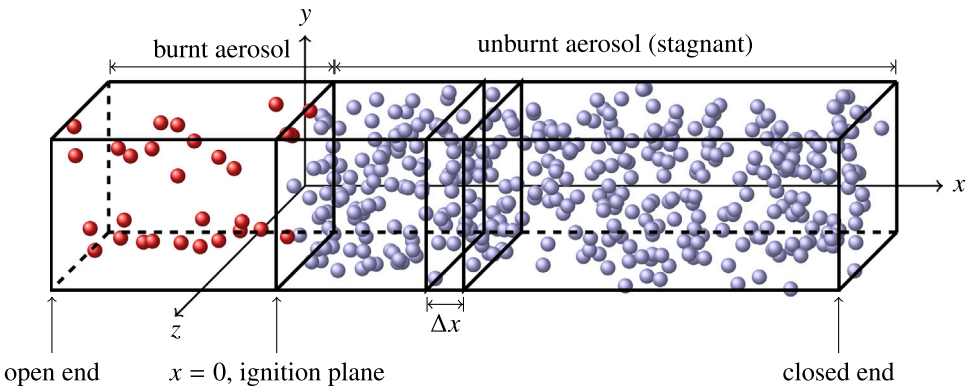

Fig. 3. Computational domain used in (quasi) 1D aerosol simulations. Blue spheres represent unburnt particles, red spheres represent burnt particles. (For interpretation of the references to colour in this figure legend, the reader is referred to the web version of this article.)

distances range between 59 μm for powder A and 551 μm for powder D. The quiescent suspension was subsequently ignited by means of an electrical coil and the resulting flame was recorded by optical tracking of radiating iron particles by a video camera running at 30 frames/s.

3.2. Numerical set-up for one-dimensional simulations

The computational domain is composed of a rectangular volume, schematically depicted in Fig. 3. For simulations in which radiation is neglected, the domain length in x-direction is determined by simulation duration t_{sim} and the expected value for u_f. For powder A, t_{sim} is set to 0.4 s and $u_f \approx 15$ cm s^{-1} is expected (from 1D simulations using Chem1D-Fe), resulting in a minimal domain length containing unburnt powder of 6 cm. For powders B, C and D, t_{sim} is increased step-wise to 1 s. In simulations 125% of this domain length containing unburnt powder is used, supplemented by a domain length of 0.5 cm containing burnt aerosol. The interface between unburnt and burnt aerosol is the starting point from where the flame will propagate through the unburnt aerosol.

If thermal radiation is included, the required domain length increases dramatically: in order to attain a negligible spatial gradient in the G-field in x-direction, and thereby no radiative heat flux in this direction, the domain is extended with three times L_{opt} on both the unburnt and burnt side. L_{opt} is estimated using Eq. (3): for powder A at $C_p = 1.1$ kg m^{-3} it ranges between 2.0 cm in the unburnt part and 7.4 cm in the burnt part due to thermal expansion of the continuous phase. If t_{sim} is set to 0.15 s and $u_f \approx 100$ cm s^{-1} according to Eq. (2), a minimal unburnt domain length of 21 cm and minimal burnt domain length of 22.5 cm is required. Used numerical grids contain 1 cell in y- and z-direction, while in x-direction the domain length is discretised with $\Delta x = 25$ μm, which is well below the expected flame thickness of approximately 1 mm [17]. The width is equal to the height of the domain, *i.e.* $\Delta y = \Delta z$ and is chosen such that each cell contains at least a few hundred individual particles to ensure sufficiently smooth fields for a_p, σ_p and source terms in the continuous phase required by the numerical solvers. In order to resolve the oxidation proces of the smallest particles in time, Δt ranges between 1 and 5 μs for powders A to D in simulations excluding thermal radiation. In simulations including thermal radiation Δt is reduced by a factor 2 since particles attain higher temperatures, as will been shown further on in this section, and therefor burn faster. This set-up results in finite-volume meshes containing up to 25 thousand cells and 23 million individual particles. To reduce simulation wall-clock time, simulations were run in parallel in which the computational domain was decomposed in 16 blocks in x-direction.

The right part of the domain, with $x \geq 0$ m, is initialised with unburnt aerosol ($Y_{g,O_2} = 0.233$, $Y_{g,N_2} = 0.767$, $Y_{p,Fe} = 1.0$ and $T_g = T_p = 300$ K) and is depicted by blue particles in Fig. 3. This part of the domain is closed off by a wall on its right boundary which assumes a no-slip boundary condition for u_g, is kept at 300 K, and employs the Marshak boundary condition described by Eq. (38) for G. Neumann boundary conditions are imposed for all variables at this boundary. The left part of the domain, with $x < 0$ m, is initialised with burnt aerosol ($Y_{g,N_2} = 1.0$, $Y_{p,FeO} = 1.0$ and $T_g = T_p = T_{eq}$ K), indicated by red particles in Fig. 3. T_{eq} represents the chemical equilibrium temperature computed by Cantera: for $C_p = 1.1$ kg m^{-3} a T_{eq} of 2178 K is obtained. This part of the domain has an open end through which burnt aerosol can escape on its boundary to the left. Neumann boundary conditions are imposed here for all variables except for the wave-transmissive boundary condition for p. Gas and particles are initially assumed to be stagnant throughout the entire computational domain and periodic boundary conditions are used in both y- and z-direction. The flame front velocity is extracted by tracking the location at which $T_g = 1250$ K in time, its temporal derivative represents the flame propagation velocity. After an initial flame development phase a steadily propagating aerosol flame was established, and time-averaging of u_f commenced.

3.3. Results for one-dimensional simulations

Results for (time-averaged) values of u_f for $C_p = 1.1$ kg m^{-3} are depicted in Fig. 4. It can be seen that simulations without radiation predict values for u_f a factor two to three smaller than observed in measurements. Predictions for u_f obtained using the OpenFOAM code deviate 8% or less from predictions made by Chem1D-Fe, and are consistent with values obtained using Eq. (1). Results for $C_p = 0.9$ kg m^{-3} and 1.3 kg m^{-3} showed practically identical results as obtained using Chem1D-Fe (presented in Section 1.1). For powder A, u_f increases by approximately 5% when C_p is lowered from 1.1 to 0.9 kg m^{-3} and decreases by approximately 5% when C_p is increased from 1.1 to 1.3 kg m^{-3}. The sensitivity of u_f with respect to C_p decreased even further with increasing d_p. From these values it can be concluded that the uncertainty in C_p in the experiments does not have a significant influence on the (predicted) value of u_f.

If radiative heat transfer is included in the simulations, predicted values for u_f are significantly larger than those observed in measurements, but in line with values obtained using Eq. (2). Flames now propagate with a time-averaged value of approximately 1.5 m s^{-1} and a standard deviation of 10% of this value; no significant difference is observed between powder A and B. For powder A, C_p is varied between 0.9 kg m^{-3} and 1.3 kg m^{-3} in these simulations as well, and predictions for u_f now exhibit a stronger dependence on C_p. Increasing C_p from 0.9 to 1.3 kg m^{-3} resulted in a reduction of u_f from 1.54 to 1.16 m s^{-1}. Due to intractable numbers of particles and grid cells, simulations for powders C and D including thermal radiation have been omitted.

Besides u_f the flame structure changes dramatically if radiative heat transfer is accounted for as shown in Fig. 5. If radiative heat

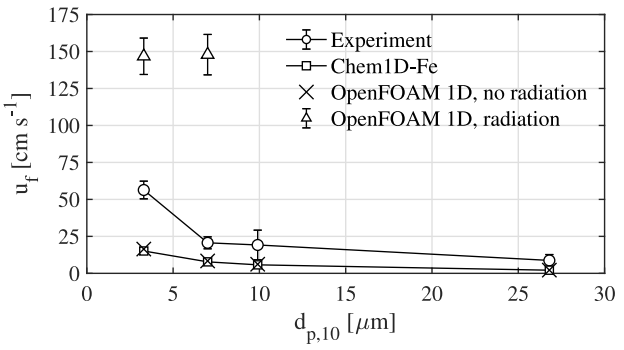

Fig. 4. Predicted flame propagation velocities in 1D with and without radiation for C_p = 1.1 kg m^{-3}. Errorbars represent RMS values.

transfer is omitted in the simulation, flame structures are observed in which conductive heat transfer in the continuous phase preheats the particles until they exhibit thermal run-away as previously described by Hazenberg et al. [17]. This implies that T_g exceeds T_p in the preheat zone in front of the reaction layer. The subsequent overshoot of T_p with respect to T_g in the reaction layer is equilibrated in the tail of the flame by means of convective heat transfer between burnt particles and carrier gas. In a theoretical analysis Goroshin et al. [62] postulated that for rich aerosols, $T_{p,max}$ should not exceed $T_{g,max}$, and this behaviour is indeed observed in the left graph of Fig. 5. This figure also shows that the predicted temperature of the burnt aerosol exceeds the value computed in chemical equilibrium calculations by approximately 100 K. This inaccuracy most likely stems from omitting the sensible enthalpy contribution in $Q_{p,reac}$ in Eq. (20). For further development of the numerical procedure it is recommended to replace Eq. (18) by an enthalpy equation for particles thereby circumventing the need to use the c_p' defined in Eq. (19) as well as $Q_{p,reac}$ defined in Eq. (20). T_p could then be looked-up from a table correlating particle enthalpy, Y_{Fe} and Y_{FeO} with T_p, thereby avoiding the need to repetitively evaluate thermodynamic polynomials.

If radiative heat transfer is accounted for in the simulation, particles in the preheat zone are predominantly heated by radiating burnt particles until they exhibit thermal run-away. The flame structure now becomes similar to the structure observed by Joulin [63] in a gaseous flame seeded with inert particles: in these experiments a gaseous fuel-oxidiser mixture was preheated by radiative heat transfer between hot and cold particles. The (homogeneous) combustion proces thereby achieved super-adiabatic flame temperatures before cooling down to its equilibrium temperature. In the current simulations, where the dispersed phase is the fuel contrary to the experiments by Joulin, particles are heated from 300 K to their ignition temperature $T_{p,ign}$ in the preheat zone. T_p exceeds T_g in this region, opposite to what is observed in simulations excluding radiative heat transfer. The ignition temperature can be estimated by equating convective heat losses with $Q_{p,reac}$ in Eq. (20) for $Da^\star \ll 1$. Making use of Semenov's criterion for ignition [64] the algebraic expression (see Appendix C for its derivation) for the ignition temperature of a particle is obtained:

$$T_{p,ign}^{-1} = \left(-\frac{3}{T_A}\right) W_{-1}\left[-\frac{1}{3}\sqrt[3]{\frac{Nu\ \lambda_f\ R_u\ T_A^2}{-2e M_{FeO}\ \Delta h^0_{FeO}\ p\ X_{O_2,g}\ k\ d_p}}\right], \tag{40}$$

in which W_{-1} denotes the Lambert function. For a particle with d_p = 3.3 μm, the $d_{p,10}$ of powder A, assuming Nu = 2 and λ_f = 51.78 mW m^{-1} K^{-1} (air at 750 K) this results in $T_{p,ign}$ = 854 K. After ignition, preheated particles reach super-equilibrium temperatures before cooling down by exchanging heat with the continuous phase, similar to the observations in experiments by Joulin. Although the domain length is chosen such that there is a distance of at least three L_{opt} between the reactive layer and both the wall on the right side as well as the outflow on the left side, $\frac{\partial G}{\partial x}$ will not be exactly zero at either of these boundaries resulting in a small energy leak. This explains why the temperature of the burnt aerosol is slightly lower for the simulations including thermal radiations and how this error can be minimised by extending the computational domain.

Comparing the obtained value for $T_{p,ign}$ with predictions made by the dedicated particle ignition model proposed by Mi et al. [48], it is seen that the value predicted by Eq. (40) lies 100 to 200 K lower than typical values obtained by Mi et al. Eq. (1) indicates that a higher $T_{p,ign}$ than predicted by Eq. (40) will result in an even more severe underestimation of u_f when radiation is not taken into account. On the other hand, Eq. (2) indicates that an elevated value for $T_{p,ign}$ will result in a better match between experiments and simulations including radiative heat transfer. It can be argued that the (higher) values for $T_{p,ign}$ obtained by Mi et al. would substantiate the need to include radiative heat transfer in numerical simulations.

Fig. 6 depicts the (instantaneous) velocity profiles for the simulation excluding and including radiative heat transfer. For the velocity of the continuous phase, basic homogeneous combustion theory for this 1D set-up leads to the expression $u_g(x) = u_f\left[T_g(x)/T_0 - 1\right]$. Since u_f is approximately 10 times larger when radiative heat transfer is accounted for, this basic expression explains the observed velocities for the continuous phase. It can also be seen that the greater inertia of larger particles causes these particles to lag behind the smaller particles in the reaction zone where they are accelerated by the expanding carrier gas. Radiative heat transfer causes both the continuous and discrete phase to start moving before particles have ignited due to the thermal expansion of the continuous phase in the preheat zone. This phenomena is absent in simulations excluding radiative heat transfer and might be used to identify this heat transfer mechanism in experimental data.

Fig. 7 compares the conductive and radiative heat fluxes in these 1D flames. The conductive heat flux is very similar in simulations in- or excluding radiation, but in the results including radiation the maximum value for the radiative heat flux can be seen to exceed the maximum value for the conductive heat flux by over a factor of 10. Furthermore, the length scale on which radiative heat transfer acts is a few dm, whereas the length scale associated with conductive heat transfer acts is only a few mm.

The applicable formulation for the particle Biot number Bi_p for the current aerosol flames balances external convective and radiative heat transfer with internal conductive heat transfer:

$$Bi_p = \left(\epsilon_p \sigma_{SB} T_p^3 d_p + \left[2 + 0.6\ Re_p^{1/2}\ Pr_f^{1/3}\right]\lambda_f\right)\lambda_p^{-1}, \tag{41}$$

in which the Ranz-Marshal relation can be recognised to compute the Nusselt number. The particle thermal conductivity in Eq. (41) is estimated by: $\lambda_p = Y_{p,Fe}\lambda_{Fe} + Y_{p,FeO}\lambda_{FeO}$ in which $\lambda_{Fe}(T)$ and $\lambda_{FeO}(T)$ have been measured by Ho et al. [65] and Akiyama et al. [66] and are evaluated at T_p. Fig. 8 shows that $Bi_p \ll 1$ for the unburnt particles, due to low values for T_p and relatively high values for $28.3 \leq \lambda_{Fe} \leq 83.5$ W m^{-1} K^{-1}. In burnt particles Bi_p attains values up to 0.075, caused by values of T_p up to nearly 2700 K and relatively low values for $3.1 \leq \lambda_{FeO} \leq 5.2$ W m^{-1} K^{-1}. It can be seen that some of the largest particles only attain values for Bi_p of approximately 0.01 in the burnt aerosol. Due to their long particle burn times and $C_p > C_{p,stoich}$, all oxygen is depleted before these large particles are fully converted from Fe to FeO: the remaining Fe magnifies λ_p compared to particles fully consisting of FeO. Based on Fig. 8 it is concluded that spatial temperature gradients within μm-sized particles are negligibly small throughout the entire flame and the assumption of a uniform T_p within particles is justified for this powder size. Since $Bi_p \propto d_p$, for particles with $d_p \gtrsim 25$ μm (like powder D) the assumption of small internal temperature gradients becomes questionable.

Results from (quasi-) 1D simulations have revealed the importance of radiative heat transfer in flames propagating through dense aerosols of fine (iron) powder. In the next subsections, the presence of the tube wall and resulting radiative heat loss in the experiments of Tang et al. will be included in the simulations.

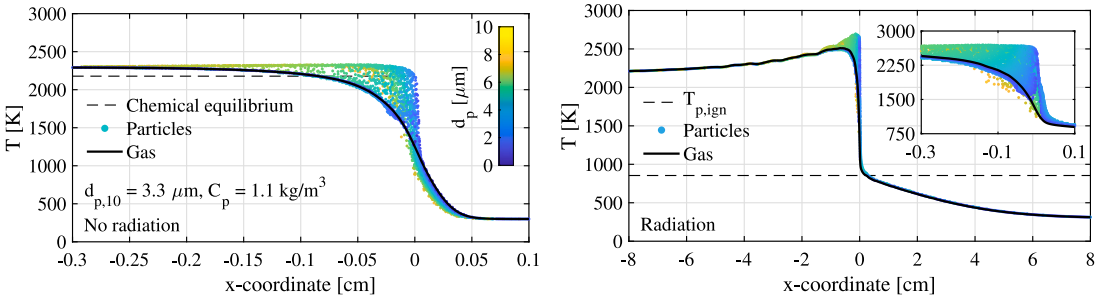

Fig. 5. Instantaneous temperature of continuous and discrete phase observed in 1D simulations of aerosol flames excluding (left graph) and including thermal radiation (right graph) for powder A at C_p = 1.1 kg m^{-3}. The depicted range in spatial coordinate in the right graph is 40 times that of the left graph; the right graph inset has the same spatial coordinates as the left graph. (For interpretation of the references to colour in this figure legend, the reader is referred to the web version of this article.)

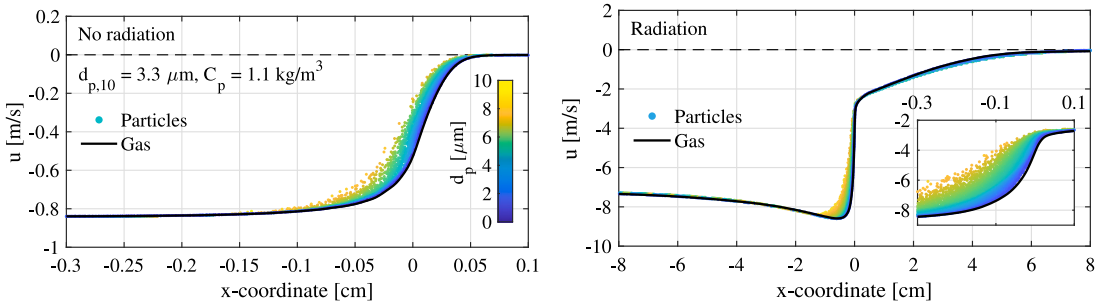

Fig. 6. Instantaneous velocity of continuous and discrete phase observed in 1D simulations of aerosol flames excluding (left graph) and including thermal radiation (right graph) for powder A at C_p = 1.1 kg m^{-3}. Spatial coordinates are identical to those in Fig. 5. (For interpretation of the references to colour in this figure legend, the reader is referred to the web version of this article.)

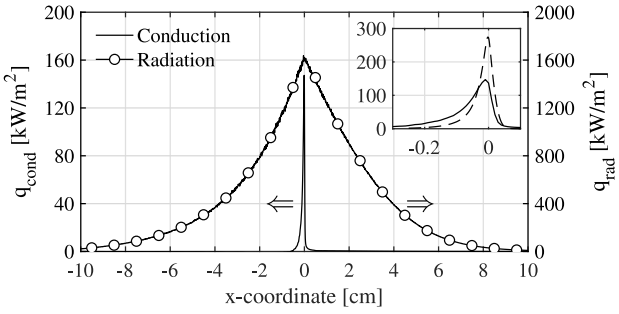

Fig. 7. Time-averaged conductive and radiative heat flux observed in 1D simulations of the aerosol flame for powder A at C_p = 1.1 kg m^{-3}. The dashed line in the inset graph represents the conductive heat flux in the simulation excluding radiation.

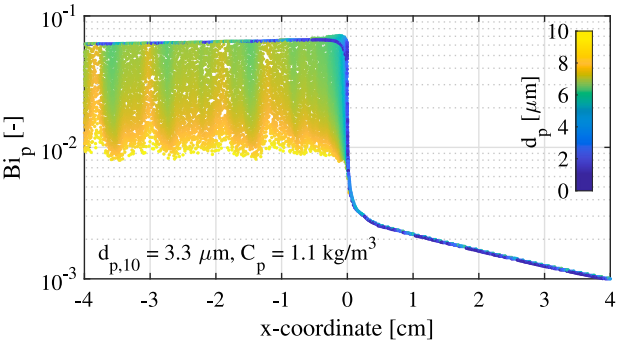

Fig. 8. Instantaneous snapshot of Bi_p-numbers observed in the 1D simulation using powder A with C_p = 1.1 kg m^{-3}. (For interpretation of the references to colour in this figure legend, the reader is referred to the web version of this article.)

3.4. Numerical set-up for three-dimensional simulations

The computational domain inside the tube is discretised by a structured O-type mesh, depicted in Fig. 9, in which the central block in the cross-section was slightly deformed in order to optimise mesh quality in terms of maximum cell skewness. Similar to the (quasi) 1D simulations, the domain is confined by an open end on its left side, the tube wall and an enclosing flat wall on its right side. The domain length in streamwise direction is determined the same way as for the 1D geometry, described in Section 3.2. Simulations not taking thermal radiation into account require a relatively short domain allowing the use of a discretisation length of Δx = 500 μm in three directions which results in 7.5 million grid cells. For the simulations including thermal radiation the required domain length is approximately 10 times the length of simulations excluding radiation to ensure that radiative heat fluxes are negligibly small at both the open end on the left side and the end-wall on the right side. In these simulations the cell length is increased to 750 μm to keep the total number of grid cells below 25 million. Given the mean inter-particle distance ranging between 59 and 551 μm for C_p = 1.1 kg m^{-3}, these values for Δx correspond to $\mathcal{O}(10^0)$ individual particles per cell for powder D to $\mathcal{O}(10^3)$ particles per cell for powder A (*i.e.* coarse to fine). For the finest two powders individual particles have been clustered in parcels, being a group of individual particles having the same value for their state variables m_p, T_p and $m_{p,k}$, to keep required computational effort within acceptable limits. In simulations without radiation each parcel of powder A contains 50 particles while for powder B this number is reduced to 5. Due to the increased domain length in simulations including radiative heat transfer, these numbers are increased to 100 and 15 respectively for these simulations. In all simulations it was checked that after clustering of particles into parcels, on average each computational cell contained 10 parcels or more.

The same limitation on Δt as in the quasi-1D simulation holds, resulting in a maximum CFL-number of $\mathcal{O}(10^{-2})$ for a grid spacing of 500 μm. The computational domain was decomposed in 2-by-2 blocks in the tube cross-section and up to 32 blocks in stream-wise direction to keep required wall-clock time below two weeks.

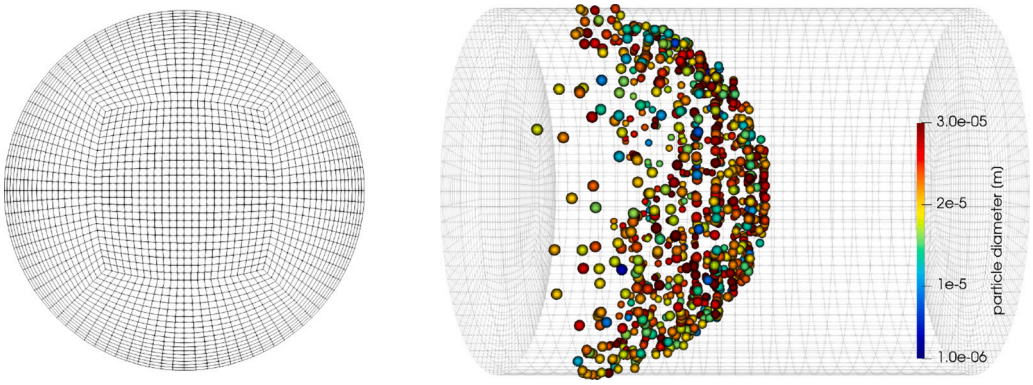

Fig. 9. Computational domain for 3D simulations. The left graph depicts the cross-section mesh topology (coarsened by a factor four for visibility). The right graph depicts the computational domain: its length in stream-wise direction depends on u_f and L_{opt}. The initial reaction layer is indicated by burning particles from powder D; particles are magnified 20 times for visibility. (For interpretation of the references to colour in this figure legend, the reader is referred to the web version of this article.)

The computational domain on the right of the half-sphere shaped flame surface depicted in Fig. 9 is initialised with unburnt aerosol while the part left of the flame surface is initialised with burnt aerosol; values for (un-)burnt aerosol properties are identical to those in the 1D simulations. For both the tube wall and enclosing end-wall the temperature is set to 300 K and no-slip boundary conditions are imposed for $u_{i,g}$. Neumann boundary conditions are imposed for the pressure field except for the wave-transmissive boundary condition at the open end. Boundary conditions for $Y_{g,k}$ consist of Neumann boundary conditions at the tube wall and open end and a Dirichlet boundary condition at the end-wall.

Like quartz glass, Pyrex is practically transparent for visible and infrared light for up to a wavelength of approximately 3.5 μm [67]: beyond this wavelength Pyrex becomes practically opaque. Since the exact optical properties are not known for the Pyrex used in the experiments, the Pyrex material is assumed to be a grey body. This assumption enables the use of the Marshak boundary condition, given in Eq. (38), to compute the radiative heat flux though the tube wall. At the open tube end a Neumann boundary condition for G is imposed, corresponding to a zero net radiative heat flux, which is justified since this boundary is located at a distance of at least three L_{opt} from the reaction layer.

In the 3D simulations the reactive layer is identified by selecting particles with $Y_{p,Fe} \in [0.5, 0.95]$ and $T_p \geq 1250$ K as depicted for powder D in Fig. 9. The flame propagation velocity is determined as the mean displacement of the 100 "most in front" burning particles in the tip of the spherical reaction layer, *i.e.* particles with the largest x-coordinate after the conditions for $Y_{p,Fe}$ and T_p have been applied. Similar to the 1D simulations time-averaging of u_f commenced when a steadily propagating aerosol flame behaviour was observed.

3.5. Results for three-dimensional simulations

Besides experimental results, Tang et al. briefly report on a comparison with a 1D numerical model. As mentioned in Section 1.1, predictions made by this 1D model were multiplied with a factor 2 to account for the parabolic flame shape. Fig. 10 shows that when radiation is not taken into account, values for u_f in 3D simulations do not show a significant increase of u_f compared to values obtained in 1D simulations. Similar to results described in Section 3.3, u_f is greatly affected by the inclusion of thermal radiation in the simulations as can be seen in Fig. 10. If radiation is accounted for, obtained values for u_f in the 3D simulations are perhaps not as high as in the 1D simulations, where $u_f \approx 150$ cm s^{-1}, but significantly higher than in 3D simulations where radiative heat transfer is neglected. As Goroshin et al. [6] point out, flames in experiments by Tang et al. are not purely radiation-driven, but based on our results we conclude that u_f is radiation-enhanced in these experiments.

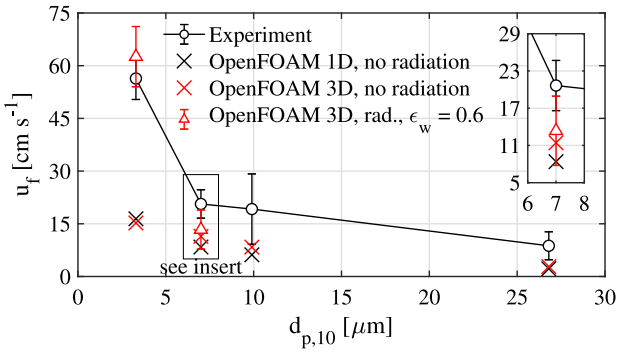

Fig. 10. Predicted flame propagation velocities in 1D simulations without radiation and 3D simulations with and without radiation for $C_p = 1.1$ kg m^{-3}. Errorbars represent RMS values.

Based on photographs of the experiment depicted in [9], simulations presented in this manuscript are initialised with a half-sphere shaped reaction layer shown in Fig. 9. However, as shown in Figs. 11 and 12, both simulations ex- and including the radiation model show that flames in aerosols created from powder A, B and C develop into quasi-flat reactive layers after reaction layer have travelled approximately one tube radius. The minor difference between the value for u_f in 1D and 3D simulations in which radiation is neglected, is most likely explained by the nearly planar reaction layer observed in the 3D simulations. The use of powder D results in a slightly concave flame: the hypothesis is raised that due to the increased reaction layer thickness heat loss to the wall has a greater effect on flame shape for this powder than for the finer powders.

A possible explanation for the difference between experimentally observed and predicted flame shapes might lie in the presence of a residual aerosol motion after injection. The used Pyrex tubes have a length of 70 cm and the dust cloud is dispersed in 10 s meaning that, at least for powder B, C and D, the injection velocity is comparable to u_f while the total aerosol density is approximately twice that of air under standard conditions. After injection, particles are only given 1 s to become motionless. In case the dust dispersion mechanism creates the highest aerosol velocity on the centreline, a toroidal flow motion might still be present when the aerosol is ignited. Aerosols created from large, *i.e.* heavy particles will then most likely exhibit more residual motion than aerosols created from small particles. This residual motion will cause additional flame front displacement: a photograph of the experiment, Fig. 5 in [9], indeed shows an increase in flame front curvature with increasing d_p. This photograph also shows that flame front curvatures are more pronounced in experiments than in

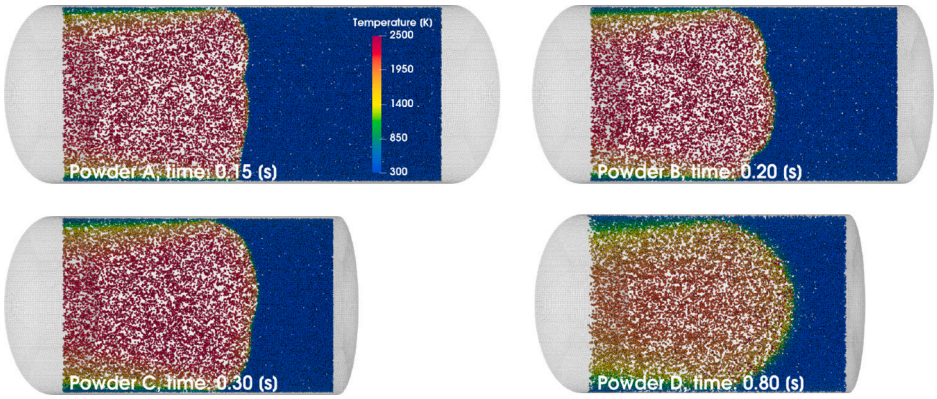

Fig. 11. Particles in tube centreline slices for aerosols created from powder A (top left), B (top right), C (bottom left) and D (bottom right) coloured by T_p. Instances in time have been chosen such that each flame front has travelled approximately half a tube diameter. Slice thicknesses are chosen such that each image contains a comparable number of parcels. (For interpretation of the references to colour in this figure legend, the reader is referred to the web version of this article.)

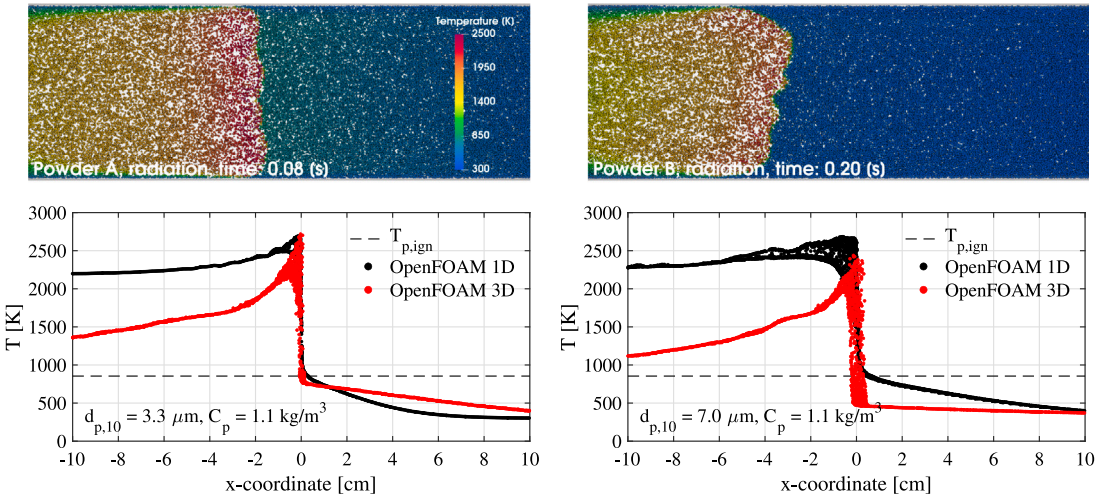

Fig. 12. Tube centreline slices for aerosols created from powder A (left column) and B (right column) using $\epsilon_w = 0.6$. The top row depicts particles in tube centreline slices similar to Fig. 11. The bottom row depict profiles for T_p in a thin cylinder with a radius of 2 mm around the tube its centreline which are compared to results from 1D simulations. (For interpretation of the references to colour in this figure legend, the reader is referred to the web version of this article.)

simulations for each powder, substantiating the hypothesis of a non-quiescent aerosol at the moment of ignition. To exclude this possible origin of deviations between experiments and simulations, it would be highly beneficial to measure aerosol motion in future experiments just prior to ignition and start simulations using these flow fields.

Besides instantaneous slices of burning aerosols created from powder A and B, Fig. 12 depicts temperature and heat flux profiles along the tube centreline. Only particles with a distance less than 2 mm from the tube centreline are used to create these profiles. As expected, the correspondence between the centreline particle temperature profile in the 3D simulation and the 1D simulation (including radiation) is better for powder A than for powder B since the first-mentioned one is optically thicker. Centreline particle temperatures the 3D simulation (including radiation) using powder B indeed follow a profile somewhere between results from 1D simulation ex- and including radiation. This is in agreement with Fig. 1, indicating that this aerosol is neither optically thick nor optically thin. Since particles from powder B are less preheated than particles from powder A when the reaction layer "arrives", maximum (super-equilibrium) values for T_p are also lower for powder B than for powder A. The more linear profile for T_p in the preheat zone of the aerosol created from powder A most likely results from an (upstream) computational domain which is too short. In case the confining wall on the right side of the domain is too close by, Eq. (36) dictates that $\partial G/\partial x < 0$, where x denotes the streamwise direction, due to the resulting radiative heat flux through the end wall. The solution of this elliptic Partial Differential Equation then results in a $q_{\mathrm{rad},x}$ which is positive in the entire preheat zone, causing T_p to rise more upstream than observed in 1D simulations. To test this hypothesis the computational domain would need to be extended further upstream which was not possible in this study due to computational limitations.

The presence of a confining wall has a great effect on the magnitude of q_{rad}: the radiative heat flux no longer dominates the conductive heat flux as depicted in Fig. 7, but attains values similar to the (maximum) value of the conductive heat flux. The magnitude of q_{rad} from the reaction layer to the unburnt particles for powder B is approximately half the value observed for powder A, which is expected since its L_{opt} in the unburnt aerosol is more than twice the value in powder A, measuring up to 135% of the tube internal diameter. Based on this observation, no significant effect of accounting for radiative heat transfer on u_f is expected for powder C and D.

As depicted in Fig. 13, for powder A with $C_p = 1.1\ \mathrm{kg\,m^{-3}}$ a good correspondence between simulations is observed for $0.5 \leq \epsilon_w \leq 0.7$, not far from the proposed value of 0.75 by Koren et al. [68]. The fact that statistics for u_f have been gathered over 50 ms most likely explains why the curve is not entirely smooth: it is expected that time-averaging over a longer time smoothens this curve. Assuming the tube wall to remain cool and thereby neglecting the radiation emitted by the tube, and inserting maximum G-values observed at the Pyrex tube wall surface, Eq. (38) tells us that maximum values for $q_{\mathrm{rad,w}}$ for this interval of ϵ_w lie slightly below 60 $\mathrm{kW\,m^{-2}}$. This value is not very impressive

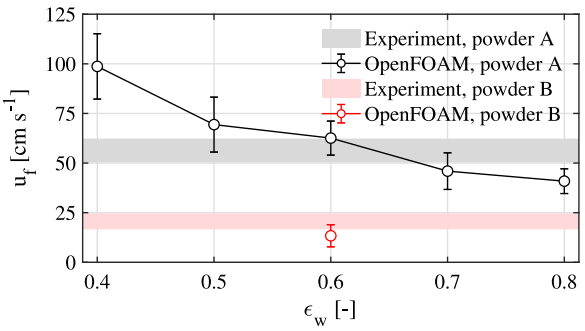

Fig. 13. Dependency of u_f on ϵ_w in 3D simulations for powders A and B with C_p = 1.1 kg m^{-3}.

when compared to Fig. 7, but considering that this heat flux acts over the tube wall over several L_{opt} results in a sink term of a few kW.

4. Conclusions and recommendations

Although several simulation tools for the prediction of u_f in oxidising iron aerosols have been presented over the last decade, all of them known to the authors underestimate experimentally observed values for u_f by a factor of two to three. This can partly be attributed to the large uncertainty in available experimental datasets: up to today it remains very hard to determine the in-situ aerosol parameters in experiments like C_p, and PSDs are typically only characterised by a $d_{p,10}$ and/or $d_{p,32}$. On the other hand, understanding and modelling of the reaction kinetics of oxidising iron particles is still at a rudimentary level and introduces a significant uncertainty comparable to experimental uncertainties.

Regardless of these uncertainties, this study demonstrates that dense iron aerosols of fine iron powders cannot always be considered to be optically thin, and that the inclusion of particle-to-particle radiative heat transfer has an influence on predicted flame speeds and flame structures that should not be overlooked. In 1D simulations of slightly fuel-rich aerosols created from fine iron powder, an increase of u_f by approximately a factor of ten is observed if radiative heat transfer is added to the model. This is explained by the radiative heat flux from burnt to unburnt aerosol which, near the reaction layer, attains values exceeding the conductive heat flux in the continuous phase by the same factor.

For the conditions identical to experiments conducted by Tang et al. it is shown that:

1. Results for u_f from 1D simulations correspond well to predictions made by Eqs. (1) and (2), in which values for u_f from simulations including radiative heat transfer are approximately ten times larger than values from simulations excluding radiation. 1D simulations mimic unconfined flames, in which no cold walls acting as heat sinks are present.
2. If radiative heat transfer is neglected, predictions of u_f from 3D simulations result in practically the same values as extracted from 1D simulations. The multiplication factor of two proposed by Tang et al. to account for the curvature of the reactive layer is not observed in the simulations, which is most likely explained by the practically planar reaction layers predicted in simulations.
3. Accounting for radiative heat transfer in the 3D simulations, including boundary conditions for the confining tube, leads to values for u_f that lay between results from 1D simulations with and without radiation. An error of 11% and 35% is obtained between predicted and measured values of u_f for powder A and B, provided that a sensible value for ϵ_w is used. This error is approximately one order of magnitude smaller than the error obtained using other established numerical tools and analytical expressions for u_f in iron aerosols.

It is recommended that numerical researchers continue developing models for iron particle oxidation to assess the influence of modelling assumptions on predictions for u_f: the possibility that overlooked aspects in current oxidation models explain the discrepancy between experiments and simulations, rather than the inclusion of radiation does, needs to be excluded. Benchmarking of numerical tools is highly recommended, given the not yet fully matured models and simulation software for aerosol combustion. Values for ϵ_p and ϵ_w should be determined with more accuracy to reduce the uncertainty in simulation outcomes caused by the uncertainty in these two input parameters. Furthermore, it is advised to examine aerosol reaction layer dynamics in confinements in greater detail to solve the disparity between the curved flame front observed in experiments, and the planar ones predicted in simulations.

Since validation of analytical and numerical tools requires accurate measurements, experimental researchers are encouraged to narrow down uncertainties in experiments. The low-hanging fruit would be to document PSDs used in experiments in a discrete manner using at least ten bins or so, to minimise the difference between actual PSDs in experiments and PSDs used in simulations. As discussed in Section 3.1, assuming a PSD described by a few statistical moments only might have a significant effect on the predicted u_f. Considering the dependence of u_f on C_p and PSD, it would be of great benefit for the iron-fuel community if the latter two parameters could be measured inside experimental combustion chambers. The authors acknowledge that these *in-situ* measurements are not a trivial task, but the knowledge of spatial distributions of C_p and PSDs would allow stricter validation of analytical and mathematical models. Last but not least, flow motion at the start of experiments, originating from the powder dispersion, should also be investigated as a possible origin for differences between experimental values for u_f and computed ones which typically assume an initially stagnant flow field. As an intermediate step, these *in-situ* measurements (C_p, PSD and flow motion after powder dispersion) could be performed under inert conditions. This allows the validation whether simulation tools can accurately reproduce the unburnt aerosol created in experiments, which seems to be a prerequisite for accurate predictions in reacting aerosols.

CRediT authorship contribution statement

W.J. S. Ramaekers: Writing – original draft, Visualization, Validation, Software, Methodology, Formal analysis, Conceptualization. **T. Hazenberg:** Writing – review & editing, Methodology, Formal analysis. **L.C. Thijs:** Writing – review & editing, Methodology. **D.J.E.M. Roekaerts:** Writing – review & editing, Methodology. **J.A. van Oijen:** Writing – review & editing, Methodology. **L.P.H. de Goey:** Writing – review & editing, Supervision, Funding acquisition.

Declaration of competing interest

The authors declare that they have no known competing financial interests or personal relationships that could have appeared to influence the work reported in this paper.

Acknowledgements

This project has received funding from the European Research Council (ERC) under the European Union's Horizon 2020 research and innovation programme under Grant Agreement no. 884916. In-depth discussions with dr. X.C. Mi were much appreciated and contributed to this paper.

Appendix A. Model constants for properties

See Tables A.1–A.3.

Table A.1
Coefficients for second-order temperature-dependent polynomials for density calculations of condensed Fe, FeO and Fe_3O_4.

	Temperature range K	$\beta_{\rho,0}$ kg m^{-3}	$\beta_{\rho,1}$ kg m^{-3} K^{-1}	$\beta_{\rho,2}$ kg m^{-3} K^{-2}	Ref.
α-Fe (s)	$275 \leq T \leq 1184$	7962.52	−0.27480	$-5.7054 \cdot 10^{-5}$	[20]
γ-Fe (s)	$1184 < T \leq 1665$	8284.36	−0.545729	0.0	[20]
δ-Fe (s)	$1665 < T \leq 1809$	8106.47	−0.464781	0.0	[20]
Fe (l)	$1809 < T \leq 3133$	8136.09	−0.61506	0.0	[20]
FeO (s)	$275 \leq T \leq 1650$	5732.52	−0.16310	$-5.7852 \cdot 10^{-5}$	[30]
FeO (l)	$1650 < T \leq 3400$	5476.28	−0.59742	0.0	[31]

Table A.2
Lennard-Jones potential parameters and Sutherland coefficients for gaseous species; k_b denotes the Boltzmann constant.

	ϵ/k_b K	σ_{LJ} Å	$\beta_{\mu,1}$ kg m^{-1} s^{-1} K$^{-0.5}$	$\beta_{\mu,2}$ K	Ref.
O_2	676.424	3.069	$2.10031 \cdot 10^{-6}$	730.549	[69]
N_2	97.839	3.610	$1.64199 \cdot 10^{-6}$	228.751	[69]
Fe (g)	3000.0	4.300	$9.82964 \cdot 10^{-7}$	1506.85	[70]
FeO (g)	3000.0	4.300	$1.11493 \cdot 10^{-6}$	1506.90	[70]

Appendix B. Effective emissivity of a semi-transparent wall

Due to lack of data on the material properties of the (semi-transparent) Pyrex material used in the experiments of Tang et al. [9,10], in this study Pyrex walls are considered to be opaque grey diffusive walls with constant emissivity. In this appendix we address the question how the emissivity used in Section 2.3 could be quantified if the necessary basic material properties of the Pyrex glass would be available.

Our analysis is based on the method developed by Rodrigues et al. [67] who state that radiative transfer through a slab of semi-transparent material can be described by solving the RTE using local material properties and taking into account the effect of interior reflections at front face and back face. This leads to equations for the amount of energy passing a slab of a certain thickness as characterised by the three coefficients: absorptance $\mathcal{A}_\lambda$, reflectance $\mathcal{R}_\lambda$ and transmittance $\mathcal{T}_\lambda$, which sum up to unity. The subscript λ refers to the wavelength and indicates that these three coefficients are wavelength-dependent. Rodrigues et al. report values for a slab of Corning HPFS 7980 quartz glass with a thickness 1 cm: this slab was found to be almost fully transparent (*i.e.* $\mathcal{T}_\lambda > \mathcal{A}_\lambda, \mathcal{R}_\lambda$) for near infrared radiation with $\lambda \leq 2.5$ μm while for far infrared radiation with $\lambda \geq 4.0$ μm $\mathcal{T}_\lambda$ drops to zero. Pyrex (borosilicate glass) is expected to have similar properties.

The radiative heat flux at wavelength λ at the inside wall of the Pyrex cylinder can be obtained from the balance of irradiance H_λ (energy approaching the wall) and radiosity J_λ (energy moving away from the wall):

$$n_j \cdot q_{\lambda,j} = J_\lambda - H_\lambda, \tag{B.1}$$

in which n_j denotes the wall normal vector, $q_{\lambda,j}$ the wavelength-dependent radiative heat flux wall at the wall and the Einstein summation convention is used over index j. The radiosity J_λ consists of the reflected part of H_λ, given by $\mathcal{R}_\lambda H_\lambda$, and the blackbody radiation emitted by the slab given by $\epsilon_\lambda E_{bb,\lambda}$, with $E_{bb,\lambda}$ being the temperature dependent Planck-curve. In addition, a part of the radiative heat flux can be transmitted from the backside of the slab $\mathcal{T}_\lambda H^0_\lambda$ where H^0_λ denotes the irradiation of the backside; this contribution is expected to be very small and is neglected here. In the considered experiment local thermodynamic equilibrium is assumed to hold, and Kirchhoff's law is valid: $\epsilon_\lambda = \mathcal{A}_\lambda$. The radiative heat flux normal to the tube wall can then be expressed as

$$\begin{aligned} n_j \cdot q_{\lambda,j} &= \left(\epsilon_\lambda E_{bb,\lambda} + \mathcal{R}_\lambda H_\lambda\right) - \left(\mathcal{A}_\lambda + \mathcal{T}_\lambda + \mathcal{R}_\lambda\right) H_\lambda \\ &= \epsilon_\lambda E_{bb,\lambda} - \left(\mathcal{A}_\lambda + \mathcal{T}_\lambda\right) H_\lambda, \end{aligned} \tag{B.2}$$

in which the identity $\mathcal{A}_\lambda + \mathcal{T}_\lambda + \mathcal{R}_\lambda = 1$ is used. In order to obtain information on total radiative heat flux, Eqs. (B.1) and (B.2) are integrated over λ, leading to equations

$$n_j \cdot q_j = J - H, \tag{B.3}$$

$$n_j \cdot q_j = \epsilon E_{bb} - (\mathcal{A} + \mathcal{T}) H, \tag{B.4}$$

in which $E_{bb} = 4\sigma_{SB} T^4_{wall}$, H denotes the total irradiation and standard definitions of total radiative properties have been used, *e.g.*

$$\epsilon = E_{bb}^{-1} \int_0^\infty \epsilon_\lambda E_{bb,\lambda} \mathrm{d}\lambda, \tag{B.5}$$

$$\mathcal{A} = H^{-1} \int_0^\infty \mathcal{A}_\lambda \mathcal{H}_\lambda \mathrm{d}\lambda. \tag{B.6}$$

Combining Eqs. (B.3) and (B.4) allow the isolation of H:

$$H = -\left(J - \epsilon E_{bb}\right) / \left(\mathcal{A} + \mathcal{T} - 1\right). \tag{B.7}$$

Substitution of this expression for H in Eq. (B.4) results in an expression for the total radiosity:

$$J = \left[\frac{\epsilon}{\mathcal{A} + \mathcal{T}}\right] E_{bb} + \left[1 - \frac{1}{\mathcal{A} + \mathcal{T}}\right] n_j \cdot q_j. \tag{B.8}$$

In the context of the P_1-model this expression for J can be substituted in the Marshak boundary condition (see Modest [54], Eq. (16.47)):

$$2 n_j \cdot q_j = 4J - G, \tag{B.9}$$

resulting in an expression for the wall normal radiative heat flux:

$$n_j \cdot q_j = \frac{\epsilon E_{bb} - (\mathcal{A} + \mathcal{T}) G}{4 - 2(\mathcal{A} + \mathcal{T})}. \tag{B.10}$$

This equation has a similar form as the Marshak boundary condition for an opaque grey wall given by Eq. (38). For the limit of a non-transmitting wall, *i.e.* $\mathcal{T} \to 0$, and imposing grey properties $\mathcal{A} = \epsilon$, Eq. (B.10) for a semi-transparent wall becomes identical to the opaque grey wall formulation, as it should. In general one cannot obtain such an agreement since ϵ_w in Eq. (38) cannot be equal to both ϵ and $\mathcal{A}+\mathcal{T}$. However, in the special case of a sufficiently cold wall, E_{bb} becomes negligibly small and the assumption that $\epsilon_w \approx \mathcal{A} + \mathcal{T}$ is appropriate. For this specific condition, Eq. (B.10) becomes equivalent to Eq. (38).

In the detailed study by Rodrigues et al. for the case of a wall of Corning HPFS 7980 quartz glass, it was found that although $\mathcal{A}$ and $\mathcal{T}$ are strongly wavelength-dependent, their sum only depends weakly on λ. For a wall thickness of 3 mm Rodrigues et al. obtained $\mathcal{A}+\mathcal{T} \approx 0.95$. Before comparing this value with the results presented in Section 3.5 it should be pointed out that the results of Rodrigues et al. concern the coefficients for a beam propagating orthogonal to the slab: the reported $\mathcal{A}_\lambda$ and $\mathcal{T}_\lambda$ are the normal absorptance and normal transmittance coefficients. For use in the radiative wall boundary condition the corresponding hemispherical quantities are needed. Both quartz glass and Pyrex have a refractive index slightly above 1.5: for this value the hemispherical emissivity is lower than the normal emissivity by about 5% (see Modest [54], Figure 3.10, case $k \approx 0$), leading to $\epsilon_w \approx 0.9$. This value is higher than the range for ϵ_w presented in Section 3.5 resulting in the best match for u_f between experiments and numerical simulations: to address this minor mismatch the first step would be to measure or compute $\mathcal{A}$ and $\mathcal{T}$ for the Pyrex tube used in the experiments. Nevertheless, this section shows that the Marshak boundary condition in Eq. (38) can be applied to semi-transparent walls like it can for opaque grey walls provided that the wall remains cold.

Appendix C. Derivation of particle ignition temperature

Ignition of particles can occur if the heat release due to oxidation exceeds heat losses. Since this process occurs at relatively low temperatures it is assumed to be limited by chemical kinetics, *i.e.* $r_r \ll r_{d,O_2}$, and for unburnt particles $A_r \approx A_p$. Furthermore the assumption is made that $T_f \approx T_p$. Eqs. (13) and (20) lead to the balance:

$$-2M_{FeO} \Delta h^0_{FeO} \left[\frac{p}{R_u T_p}\right] X_{g,O_2} k \exp\left(-\frac{T_A}{T_p}\right) = N u \lambda_f d_p^{-1} \left(T_p - T_g\right) \tag{C.1}$$

Table A.3
Polynomial coefficients to calculate discrete phase density using Equation (23).

	Escaping gas	From liquid	Temperature range K	$\beta_{vap,1}$	$\beta_{vap,2}$	$\beta_{vap,3}$
$p_{vap,I}$	Fe (g)	Fe (l)	$1809 < T \leq 3133$	35.40	$-4.963 \cdot 10^4$	−2.433
$p_{vap,II}$	Fe (g)	FeO (l)	$1650 < T \leq 3400$	62.08	$-6.412 \cdot 10^4$	−5.399
$p_{vap,III}$	FeO (g)	FeO (l)	$1650 < T \leq 3400$	52.93	$-6.480 \cdot 10^4$	−4.370

Introducing

$$T_p = T_g(1+\epsilon\theta) = T_g\frac{(1+\epsilon\theta)(1-\epsilon\theta)}{(1-\epsilon\theta)} \approx T_g\frac{1}{(1-\epsilon\theta)} \quad \text{with} \quad \epsilon = T_g/T_A \ll 1 \tag{C.2}$$

Eq. (C.1) can be recast to:

$$\exp\theta = \underbrace{\left[\frac{Nu\lambda_f R_u}{-2M_{FeO}\Delta h^0_{FeO} p X_{g,O_2} k d_p}\right]\exp\left(\frac{T_A}{T_g}\right)\left(\frac{T_g^3}{T_A}\right)}_{=\beta}\theta. \tag{C.3}$$

Semenov's criterion [64] states that for ignition the following conditions must be met:

$$\exp\theta = \beta\theta \tag{C.4}$$

$$\frac{d}{d\theta}(\exp\theta) = \frac{d}{d\theta}(\beta\theta) \rightarrow \exp\theta = \beta \tag{C.5}$$

which has the unique solution $\theta = 1$ and $\beta = \exp(1) = e$. This leads to the expression for $T_{p,ign}$:

$$\frac{T_A^3}{T_{p,ign}^3}\exp\left(-\frac{T_A}{T_{p,ign}}\right) = \left[\frac{Nu\lambda_f R_u T_A^2}{-2M_{FeO}\Delta h^0_{FeO} p X_{g,O_2} k d_p}\right] \tag{C.6}$$

which is, with some algebra, recast to:

$$-\frac{T_A}{3T_{p,ign}}\exp\left(-\frac{T_A}{3T_{p,ign}}\right) = -\frac{1}{3}\left[\frac{Nu\lambda_f R_u T_A^2}{-2M_{FeO}\Delta h^0_{FeO} p X_{g,O_2} k d_p}\right]^{1/3}. \tag{C.7}$$

Eq. (C.7) can be solved by the Lambert W_{-1} function:

$$-\frac{T_A}{3T_{p,ign}} = W_{-1}\left[-\frac{1}{3}\sqrt[3]{\frac{Nu\lambda_f R_u T_A^2}{-2eM_{FeO}\Delta h^0_{FeO} p X_{O_2,g} k d_p}}\right] \tag{C.8}$$

provided that

$$-\frac{1}{e} \leq \left[-\frac{1}{3}\sqrt[3]{\frac{Nu\lambda_f R_u T_A^2}{-2eM_{FeO}\Delta h^0_{FeO} p X_{O_2,g} k d_p}}\right] < 0. \tag{C.9}$$

Eq. (C.8) can subsequently simply be recast to Eq. (40).

References

[1] D.B. Beach, A.J. Rondinone, B.G. Sumpter, S.D. Labinov, R.K. Richards, Solid-state combustion of metallic nanoparticles: new possibilities for an alternative energy carrier, J. Energy Resour. Technol. 129 (1) (2006) 29–32.

[2] J.M. Bergthorson, Recyclable metal fuels for clean and compact zero-carbon power, Prog. Energy Combust. Sci. 68 (2018) 169–196.

[3] J.M. Bergthorson, S. Goroshin, M.J. Soo, P. Julien, J. Palečka, D.L. Frost, D. Jarvis, Direct combustion of recyclable metal fuels for zero-carbon heat and power, Appl. Energy 160 (2015) 368–382.

[4] E. Mallard, H. Le Châtelier, Sur les vitesses de propagation de l'inflammation dans les mélanges gazeux explosifs, Acad. des Sci. 93 (1881) 141–148.

[5] D. Ning, Y. Shoshin, J.A. van Oijen, G. Finotello, L.P.H. de Goey, Burn time and combustion regime of laser-ignited single iron particle, Combust. Flame 230 (2021) 111424.

[6] S. Goroshin, J. Palečka, J.M. Bergthorson, Some fundamental aspects of laminar flames in nonvolatile solid fuel suspensions, Prog. Energy Combust. Sci. 91 (2022) 100994.

[7] J.H. Sun, R. Dobashi, T. Hirano, Structure of flames propagating through metal particle clouds and behavior of particles, Symp. (Int.) Combust. 27 (2) (1998) 2405–2411.

[8] J.H. Sun, R. Dobashi, T. Hirano, Combustion behavior of iron particles suspended in air, Combust. Sci. Technol. 150 (1–6) (2000) 99–114.

[9] F.D. Tang, S. Goroshin, A. Higgins, J. Lee, Flame propagation and quenching in iron dust clouds, Proc. Combust. Inst. 32 (2009) 1905–1912.

[10] F.D. Tang, S. Goroshin, A. Higgins, Modes of particle combustion in iron dust flames, Proc. Combust. Inst. 33 (2) (2011) 1975–1982.

[11] A. Wright, A.J. Higgins, S. Goroshin, The discrete regime of flame propagation in metal particulate clouds, Combust. Sci. Technol. 188 (11–12) (2016) 2178–2199.

[12] M. Fedoryk, B. Stelzner, S. Harth, D. Trimis, Experimental investigation of the laminar burning velocity of iron-air flames in a tube burner, Appl. Energy Combust. Sci. 13 (2023) 100111.

[13] S. Goroshin, F.D. Tang, A.J. Higgins, Reaction-diffusion fronts in media with spatially discrete sources, Phys. Rev. E 84 (2) (2011) 027301.

[14] X. Wen, A. Scholtissek, J.A. van Oijen, J.M. Bergthorson, C. Hasse, Numerical modeling of pulverized iron flames in a multidimensional hot counterflow burner, Combust. Flame 248 (2023) 112572.

[15] M.J. Soo, K. Kumashiro, S. Goroshin, D.L. Frost, J.M. Bergthorson, Thermal structure and burning velocity of flames in non-volatile fuel suspensions, Proc. Combust. Inst. 36 (2) (2017) 2351–2358.

[16] J. Mich, D. Braig, T. Gustmann, C. Hasse, A. Scholtisekk, A comparison of mechanistic models for the combustion of iron microparticles and their application to polydisperse iron-air suspensions, Combust. Flame 256 (2023) 112949.

[17] T. Hazenberg, J.A. van Oijen, Structures and burning velocities of flames in iron aerosols, Proc. Combust. Inst. 38 (3) (2021) 4383–4390.

[18] W. Nusselt, Der verbrennungsvorgang in der kohlenstaubfeuerung, Ver. Deut. Ing. 68 (1924) 124–128.

[19] M. Muller, H. El-Rabii, R. Fabbro, Liquid phase combustion of iron in an oxygen atmosphere, J. Mater. Sci. 50 (9) (2015) 3337–3350.

[20] K. Thurnay, Thermal Properties of Transition Metals, Tech. Rep. FZKA 6095, Forschungszentrum Karlsruhe, Germany, 1998.

[21] F. Lam, X.C. Mi, A.J. Higgins, Front roughening of flames in discrete media, Phys. Rev. E 96 (1) (2017) 013107.

[22] F. Lam, X.C. Mi, A.J. Higgins, Dimensional scaling of flame propagation in discrete particulate clouds, Combust. Theory Model. 24 (3) (2020) 486–509.

[23] M.J. Soo, S. Goroshin, J.M. Bergthorson, D.L. Frost, Reaction of a particle suspension in a rapidly heated oxidizing gas, Propellants Explos. Pyrotech. 40 (2015) 604–612.

[24] V.A. Vlasov, E.N. Lysenko, A.P. Surzhikov, S. Zhuravkov, A.V. Pustovalov, N. Yavorovsky, The oxidation kinetics study of ultrafine iron powders by thermogravimetric analysis, J. Therm. Anal. Calorim. 115 (2014) 1447–1452.

[25] M. Schiemann, P. Fischer, J.M. Bergthorson, Iron particles as carbon-neutral fuel in spray roasting reactors, in: Proc. of the 8th European Combust. Meeting, 2017, pp. 487–492.

[26] C.E.A.G. van Gool, L.C. Thijs, W.J.S. Ramaekers, J.A. van Oijen, L.P.H. de Goey, Particle equilibrium composition model for iron dust combustion, Appl. Energy Combust. Sci. 13 (2023) 100115.

[27] I. Glassman, R.A. Yetter, Combustion, Academic Press, 2008.

[28] R.A. Yetter, G.A. Risha, S.F. Son, Metal particle combustion and nanotechnology, Proc. Combust. Inst. 32 (2009) 1819–1838.

[29] B.J. McBride, M.J. Zehe, S. Gordon, NASA Glenn Coefficients for Calculating ThermodynamicProperties of Individual Species, Tech. Rep. NASA/TP 2002-211556, National Air and Space Administration, 2002.

[30] C.W. Bale, E. Bélisle, P. Chartrand, S.A. Decterov, G. Eriksson, A.E. Gheribi, K. Hack, I.H. Jung, Y.B. Kang, J. Melançon, A.D. Pelton, S. Petersen, C. Robelin, J. Sangster, M.-A. van Ende, FactSage thermochemical software and databases, 2010–2016, CALPHAD 54 (2016) 35–53.

[31] Y.E. Lee, D.R. Gaskell, The densities and structures of melts in the system CaO-FeO-SiO_2, Metall. Mater. Trans. B 5 (1974) 853–860.

[32] M.J. Assael, K. Kakosimos, R.M. Banish, J. Brillo, I. Egry, R. Brooks, P.N. Quested, K.C. Mills, A. Nagashima, Y. Sato, W.A. Wakeham, Reference data for the density and viscosity of liquid aluminum and liquid iron, J. Phys. Chem. Ref. Data 35 (1) (2006) 285–300.

[33] R.S. Hixson, M.A. Winkler, M.L. Hodgdon, Sound speed and thermophysical properties of liquid iron and nickel, Phys. Rev. B 42 (10) (1990) 6485–6491.

[34] T. Saito, Y. Shiraishi, Y. Sakuma, Density measurement of molten metals by levitation technique at temperatures between 1800°C and 2200°C, Trans. Iron Steel Inst. Japan 9 (1969) 118–126.

[35] D.J. Steinberg, A simple relationship between the temperature dependence of the density of liquid metals and their boiling temperatures, Metall. Trans. B 5 (1974) 1341–1343.

[36] S. Watanabe, Y. Tsu, K. Takano, Y. Shiraishi, Density of pure iron in solid and liquid states, J. Japan. Inst. Metals 45 (3) (1980) 242–249.

[37] K. Mori, K. Suzuki, Density of iron oxide melt in equilibrium with CO_2-CO gas mixture, Trans. Iron Steel Inst. Jpn. 8 (1968) 382–385.

[38] A. Fujinawa, L.C. Thijs, J. Jean-Philyppe, A. Panahi, D. Chang, M. Schiemann, Y.A. Levendis, J.M. Bergthorson, X.C. Mi, Combustion behaviour of single iron particles - part II: a theoretical analysis based on a zero-dimensional model, Appl. Energy Combust. Sci. 14 (2023) 100145.
[39] G.L. Hubbard, V.E. Denny, A.F. Mills, Droplet evaporation: effects of transients and variable properties, Int. J. Heat Mass Transfer 18 (1975) 1003–1008.
[40] M.C. Yuen, L.W. Chen, On drag of evaporating liquid droplets, Combust. Sci. Technol. 14 (1976) 147–154.
[41] L.C. Thijs, C.E.A.G. van Gool, W.J.S. Ramaekers, J.G.M. Kuerten, J.A. van Oijen, L.P.H. de Goey, Improvement of heat- and mass transfer modeling for single iron particles combustion using resolved simulations, Combust. Sci. Technol. 196 (4) (2022) 572–588.
[42] L. Schiller, Z. Naumann, A drag coefficient correlation, Z. Ver. Deutsch. Ing. 77 (1935) 318–320.
[43] M. Sommerfeld, Particles in Flows, Springer International Publishing, 2017, pp. 327–396.
[44] D.G. Goodwin, R.L. Speth, H.K. Moffat, B.W. Weber, Cantera: An object-oriented software toolkit for chemical kinetics, thermodynamics, and transport processes (version 2.5.1), 2021.
[45] E.I. Senyurt, E.L. Dreizin, At what ambient temperature can thermal runaway of a burning metal particle occur?, Combust. Flame 236 (2022) 111800.
[46] J. Jean-Philyppe, A. Fujinawa, J.M. Bergthorson, X.C. Mi, The ignition of fine iron particles in the knudsen transition regime, Combust. Flame 255 (2023) 112869.
[47] L.C. Thijs, E. Kritikos, A. Giusti, W.J.S. Ramaekers, J.A. van Oijen, L.P.H. de Goey, X.C. Mi, On the surface chemisorption of oxidizing fine iron particles: Insights gained from molecular dynamics simulations, Combust. Flame 254 (2023) 112871.
[48] X.C. Mi, A. Fujinawa, J.M. Bergthorson, A quantitative analysis of the ignition characteristics of fine iron particles, Combust. Flame 240 (2022) 112011.
[49] W.E. Ranz, W.R. Marshall, Evaporation from drops, Chem. Eng. Progress 48 (3) (1952) 141–146, 173–180.
[50] B.E. Poling, J.M. Prausnitz, J.P. O'Connell, Properties of Gases and Liquids, fifth ed., McGraw-Hill Education, 2001.
[51] L.C. Thijs, C.E.A.G. van Gool, W.J.S. Ramaekers, J.A. van Oijen, L.P.H. de Goey, Resolved simulations of single iron particle combustion and the release of nano-particles, Proc. Combust. Inst. 39 (3) (2022) 3551–3559.
[52] D. Ning, Y. Shoshin, J.A. van Oijen, M. van Stiphout, G. Finotello, L.P.H. de Goey, Temperature and phase transitions of laser-ignited single iron particle, Combust. Flame 236 (2022) 111801.
[53] M.A. Liberman, Combustion Physics: Flames, Detonations, Explosions, Astrophysical Combustion and Inertial Confinement Fusion, Springer International Publishing, 2021.
[54] M.F. Modest, Radiative Heat Transfer, third ed., Elsevier Science, 2013.
[55] G.K. Burgess, R.G. Waltenberg, The Emissivity of Metals and Oxides: Measurements with the Micropyrometer, Tech. Rep. vol. 11, US Dept. of Commerce, Bureau of Standards, 1915.
[56] J.M. Jones, P.E. Mason, A. Williams, A compilation of data on the radiant emissivity of some materials at high temperatures, J. Energy Inst. 92 (3) (2019) 523–534.
[57] S. Krishnan, K. Yugawa, P. Nordine, Optical properties of liquid nickel and iron, Phys. Rev. B 55 (13) (1997) 8201–8206.
[58] R.E. Marshak, Note on the spherical harmonic method as applied to the milne problem for a sphere, Phys. Rev. 71 (7) (1947) 443–446.
[59] T. Poinsot, D. Veynante, Theoretical and Numerical Combustion, R.T. Edwards Inc., 2001.
[60] A. Bukhvostova, Heat and Mass Transfer in Turbulent Multiphase Channel Flow (Ph.D. thesis), Twente University of Technology, 2015.
[61] A. Ravi, L.P.H. de Goey, J.A. van Oijen, Effect of particle size distribution on the laminar flame speed of iron aerosols, Combust. Flame 257 (2023) 113053.
[62] S. Goroshin, F.-D. Tang, A.J. Higgins, J.H.S. Lee, Quenching distance of laminar flame in aluminum dust clouds, Combust. Flame 105 (1) (1996) 147–160.
[63] G. Joulin, Temperature-lags and radiative transfer in particle-laden gaseous flames, part 1: steady planar fronts, Combust. Sci. Technol. 52 (4–6) (1987) 377–395.
[64] N.N. Semenov, The calculation of critical temperatures of thermal explosion, Z. Phys. Chem. 48 (1928) 571.
[65] C.Y. Ho, R.W. Powell, P.E. Liley, Thermal conductivity of the elements, J. Phys. Chem. Ref. Data 1 (2) (1972) 279–421.
[66] T. Akiyama, H. Ohta, R. Takahashi, Y. Waseda, J.I. Yagi, Measurement and modeling of thermal conductivity for dense iron oxide and porous iron ore agglomerates in stepwise reduction, ISIJ Int. 32 (7) (1992) 829–837.
[67] P. Rodrigues, O. Gicquel, N. Darabiha, K.P. Geigle, R. Vicquelin, Assessment of external heat transfer modeling of a laboratory-scale combustor: Effects of pressure-housing environment and semi-transparent viewing windows, J. Eng. Gas Turb. Power 141 (3) (2019) 031011.
[68] C. Koren, R. Vicquelin, O. Gicquel, Multiphysics simulation combining large-eddy simulation, wall heat conduction and radiative energy transfer to predict wall temperature induced by a confined premixed swirling flame, Flow Turbul. Combust. 101 (2018) 77–102.
[69] A.A. Konnov, Yet another kinetic mechanism for hydrogen combustion, Combust. Flame 203 (2019) 14–22.
[70] M.D. Rumminger, D. Reinelt, V. Babushok, G.T. Linteris, Numerical study of the inhibition of premixed and diffusion flames by iron pentacarbonyl, Combust. Flame 116 (1) (1999) 207–219.